National Aeronautics and Space Administration

Satellite-Based Thermal Precursors of Volcanic Eruptions

Author: Társilo Girona (329A)
Co-authors: Vincent Realmuto (329A), Paul Lundgren (329A)

1. Introduction: diffuse emissions of heat

A major challenge in natural disaster management revolves around detecting precursors of volcanic eruptions. Volcanic eruptions are preceded by the ascent of hot material to the Earth surface, although the pre-eruptive thermal footprint is subtle. Rather than looking for pre-eruptive hot spots [e.g., *1-3*], whose predictive ability remains controversial [*4*], here **we explore the diffuse emissions of heat** (Fig. 1).

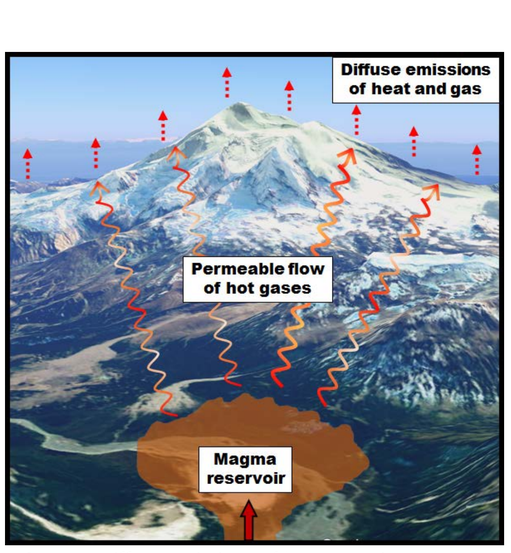

Figure 1. Diffuse emissions of heat at active volcanoes. Background image is Redoubt volcano (Google Earth).

Research Questions:

1. Do diffuse emissions of heat vary significantly before volcanic eruptions?
2. Can we forecast volcanic eruptions by monitoring diffuse emissions of heat from space?

Approach: Analysis of long-wavelength thermal infrared data retrieved from the MODIS instruments onboard Terra and Aqua satellites [*5*].

Target volcanoes: Ruapehu (New Zealand), Ontake (Japan), Redoubt (Alaska; USA), Puyehue (Chile), and Domuyo (Argentina).

2. Data processing: median-of-median algorithm

1. We retrieve radiance data (band 31: 10.780-11.280 μm) since July 1st, 2002, from the Level 1B calibrated and geolocated MODIS products with ~1x1 km pixel resolution.
2. We choose a region of interest (ROI) of ~1,000 pixels centered on the target volcano (Fig. 2A). Then, we calculate the **median radiance** emitted by the volcanic edifice (L_v^*) and surroundings (L_s^*).
3. We calculate the median of the values of L_v^* and L_s^* of every day. This produces the **daily median radiance** emitted by the volcanic edifice (L_v) and surroundings (L_s), respectively.
4. We define the Thermal Emission Difference as $\boldsymbol{TED = L_v - L_s}$ (Fig. 2B). $\boldsymbol{TED}$ **is expected to capture the warming of the volcanic edifice with respect to the surroundings**.

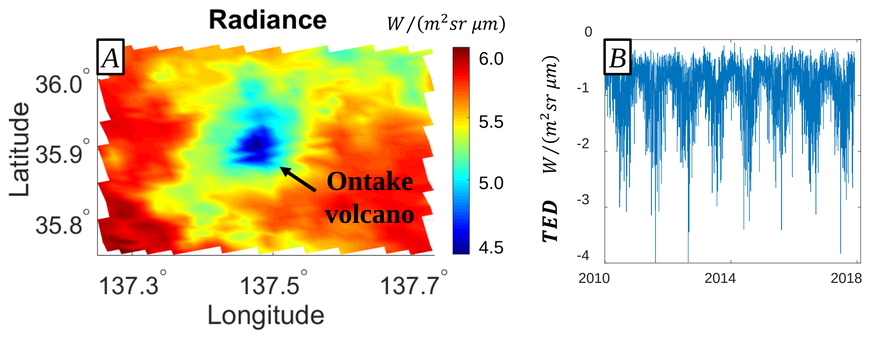

Figure 2. Data processing. **(*A*)** Example of the scenes analyzed. **(*B*)** Example of TED time series. The area covering the volcanic edifice is defined as the region with 50 to 100 pixels with lower radiance. This approach is valid as long as the volcanic edifice is colder than the surroundings due to altitude effects.

3. Montecarlo experiments: design of an efficient denoising technique

Recognizing trends of volcanic origin in TED time series is difficult due to seasonal effects and noise (Fig. 2B). To unveil long-term (~ years) trends, first we analyze through Montecarlo experiments the efficiency of several denoising techniques. Our experiments show that **a combination of wavelet and median filters is suitable to detect long-term trends** in TED time series with signal-to-noise ratio as low as ~0.1 (Fig. 3).

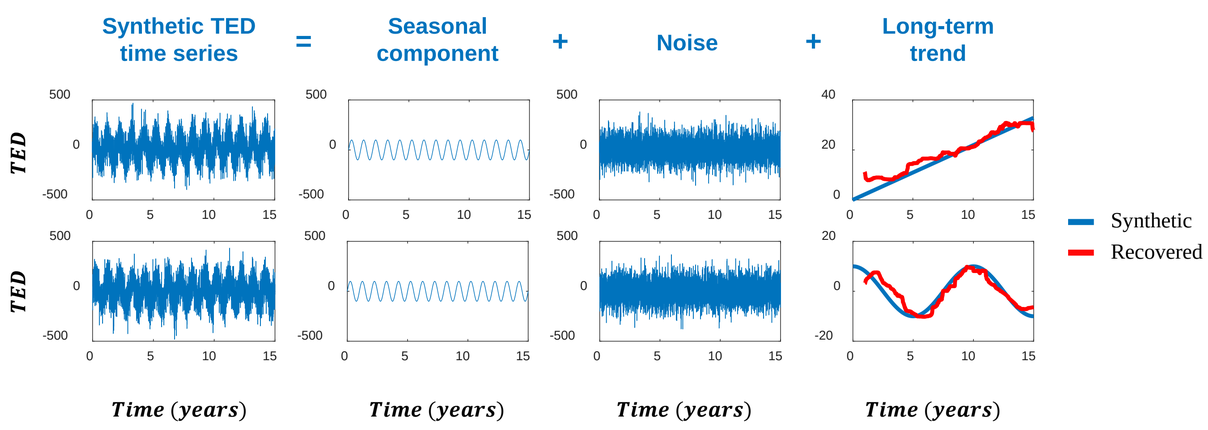

Figure 3. Examples of denoising of two synthetic TED time series (arbitrary units). Synthetic TED time series are generated by adding a periodic signal (1-year periodicity), Gaussian noise, and a linear trend (top) or sinusoidal trend (bottom). Long-term trends are recovered (red) by applying to the synthetic TED time series ten maximal overlap wavelet transform filters and a 1-year trailing moving median filter.

4. Results I: application to four active volcanoes

The denoising technique is applied to the TED data to obtain the Filtered Thermal Emission Difference ($FTED$) time series. We find that (Fig. 4):

Eruptions occurred at high values of $FTED$

Diffuse emissions of heat increased before eruptions

This likely reflects hot gas circulation in the crust and **greater diffuse degassing** [*6*] (heat conduction is not efficient)

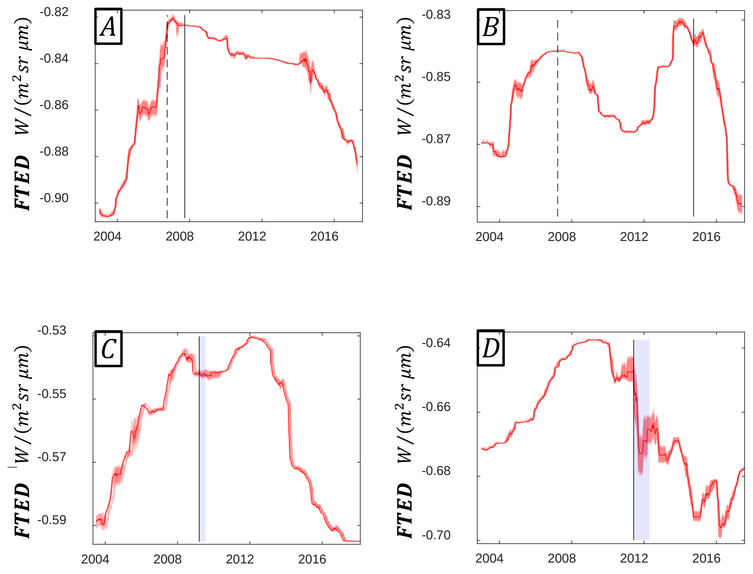

Figure 4. $FTED$ time series for: **(*A*)** Ruapehu; **(*B*)** Ontake; **(*C*)** Redoubt; and **(*D*)** Puyehue. Solid lines, dashed lines, grey shaded regions, and thickness of red lines represent the onset of major eruptions, the onset of minor explosions, eruption duration, and uncertainty (obtained with bootstrapping), respectively.

5. Results II: thermal-deformation coupling. Is magma rising to the surface?

Domuyo is a volcanic caldera that has been inflating since 2014. However, heat emissions were not concomitant and are **phase shifted** (Fig. 5A), suggesting that magma is not rising to the surface. We explore this by modeling the link between diffuse degassing and magma reservoir pressure (proxies for diffuse heat and deformation) (Fig. 1). Our preliminary results suggest that (Fig. 5B):

Permeable gas flow through the crust can produce spontaneous (and phase shifted) oscillations of heat emissions and deformation

Inflation of volcanic calderas does not necessarily mean magma ascent

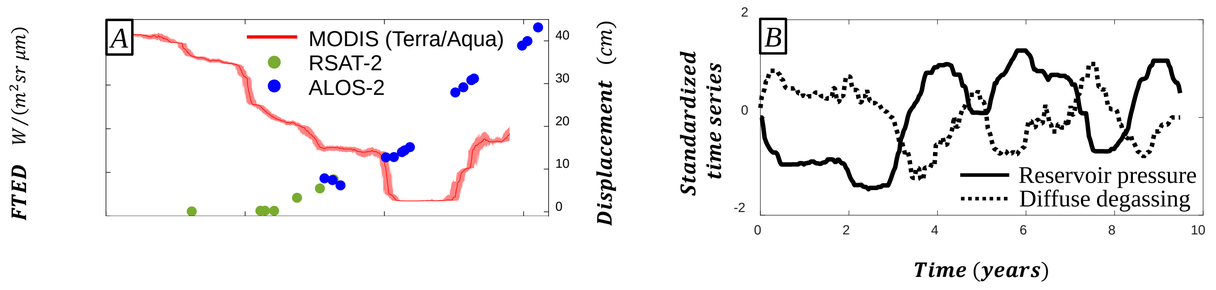

Figure 5. Thermal-deformation coupling. ***(A)*** FTED (line) and deformation (circles) times series. Inflation source is at ~6 km depth. ***(B)*** Example of the output of our forward model, which solves the Navier-Stokes equation for gas permeable flow. We assume reasonable values for the parameters involved (permeability, porosity, size and depth of magma reservoir, etc.). Details of the model can be found in [*7*, *8*].

6. Conclusions and implications for volcano monitoring

- This is the **first time that pre-eruptive diffuse emissions of heat, which is related to diffuse degassing, have been detected from space**.
- **Our methodology can be automatized to detect volcanic unrest and thus better forecast eruptions**. For example, the last eruption of Ontake volcano (2014), which killed 63 people because warning signs were not identified with traditional monitoring methods (e.g., seismicity) [*9*], could have been forecasted through satellite-based thermal monitoring (Fig. 4B).
- The **combination of our thermal infrared methodology with geodetic analysis can provide new insights on** the processes governing the dynamics of active volcanoes.

National Aeronautics and Space Administration
Jet Propulsion Laboratory
California Institute of Technology
Pasadena, California
www.nasa.gov

References:
[1] Pieri, D., Abrams, M. (2005), *Remote Sens. Environ.*, 99, 84-94. **[2]** Lacava, T., *et al.* (2014), *J-STARS,* 7, 8. **[3]** Van Manem, S.M., Dehn, J. (2009), *Geology*, 37, 11. **[4]** Blackett, M. (2017), *J. Imaging*, 3, 13. **[5]** Justice, C.O., *et al.* (1998), *IEEE Trans. Geosci. Remote Sens.*, 36, 4, 1228-1249. **[6]** Schwandner, F.M., *et al.* (2004), J. Geophys. Res. Atmos., 109, D04301. **[7]** Girona, T., Huber, C., Caudron, C. (2018), *Sci. Rep.*, 8, 1476. **[8]** Girona, T., Caudron, C., Huber, C. (submitted). **[9]** Sano, Y., et al. (2015), *Sci. Rep.*, 5, 13069.

Acknowledgments:
T. Girona is supported by an appointment to the NASA Postdoctoral Program at the NASA Jet Propulsion Laboratory, administered by Universities Space Research Association under contract with NASA.

Poster No. EA-01

National Aeronautics and Space Administration

Spatiotemporal characterization of tectonic signals from geodetic data: The 2010 El Mayor-Cucapah, Mw 7.2, post-seismic deformation

Adriano Gualandi (329A) and Zhen Liu (329A)

GOAL: Understand the connection between post-seismic deformation processes and seismic activity
DATA: Daily continuous GPS (cGPS) position time series
PROBLEM: How to separate and model multiple simultaneously active deformation signals (tectonic and non-tectonic)?
SOLUTION: Blind source separation algorithms to retrieve process related signals and model them independently

In particular, we use the variational Bayesian Independent Component Analysis (vbICA) approach (*Gualandi et al.*, 2016, *JOGE*; 2017a, *GRL*; 2017b, *GRL*; 2017c, *Tectonophysics*; *Serpelloni et al.*, 2018, *JGR*; *Nespoli et al.*, 2018, *Geofluids*)

1 - DATA

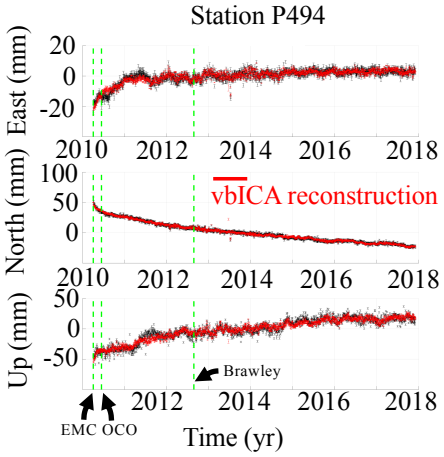

Position time series:
- Clear post-seismic deformation after El Mayor-Cucapah (EMC) earthquake
- Ocotillo (OCO) aftershock and Brawley swarm offsets corrected
- 12 Independent Components (ICs) for 125 stations, 2 ICs clearly tectonic

2 - EL MAYOR-CUCAPAH EARTHQUAKE

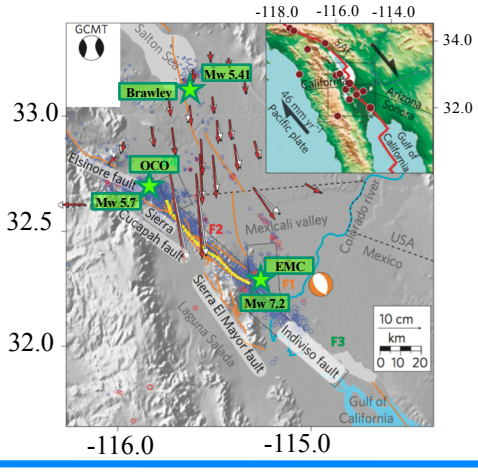

Study region, map view (modified from *Wei et al.*, 2011, *Nat. Geo.*). White/Red arrows: Horizontal data/modeled co-seismic motion. Fault geometry for modeling: extended from *Huang et al.*, 2017, *JGR*.

3 - METHODOLOGY

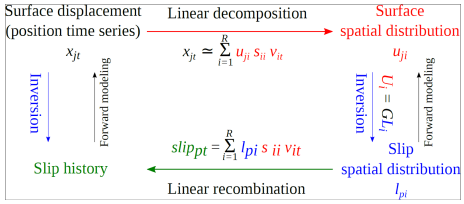

Inversion scheme (modified from *Kositsky and Avouac*, 2010, *JGR*).

4 - RESULTS AND NEXT STEP

- At least 2 ICs to explain tectonic signals
- Shallow afterslip explains rapid decay
- Deep afterslip explains slow decay horizontal displacements, but not vertical
- Seismicity cluster related to EMC: slow decay and broad region of interest
- Seismicity cluster related to OCO: rapid decay and narrow region of interest
- Future work: Viscoelastic relaxation model to fit IC_1 vertical pattern

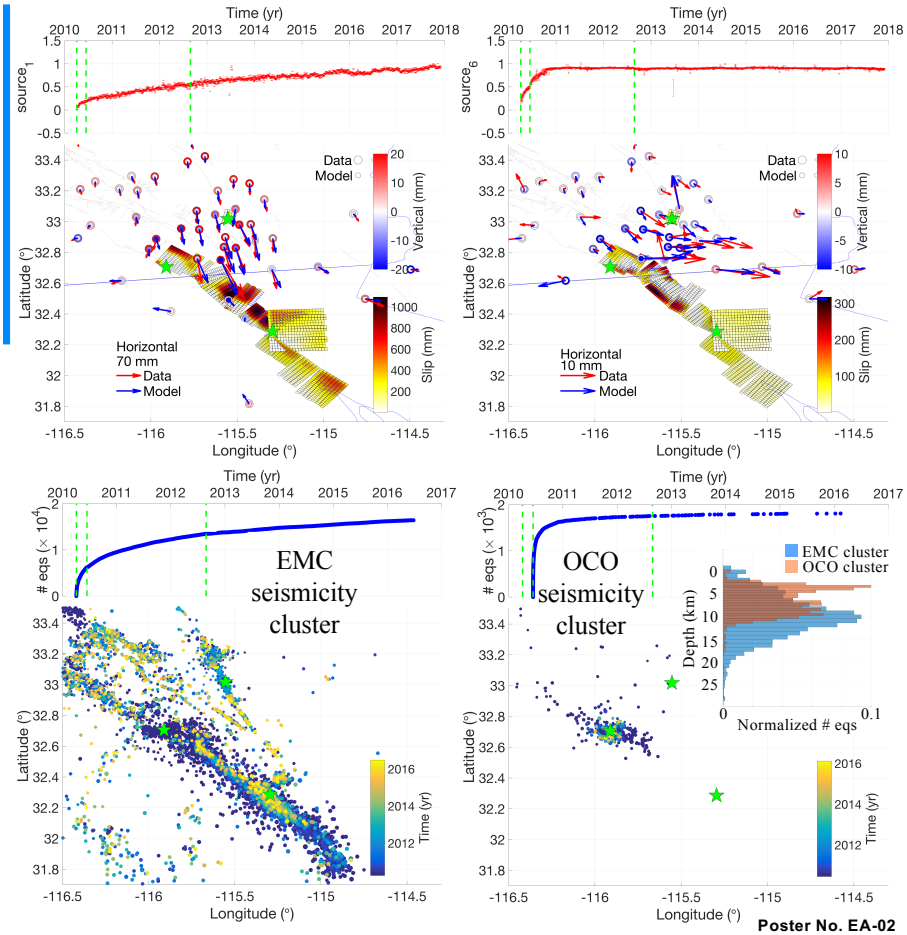

National Aeronautics and Space Administration
Jet Propulsion Laboratory
California Institute of Technology
Pasadena, California

www.nasa.gov

Poster No. EA-02

National Aeronautics and Space Administration

A Shift from Drought to Extreme Rainfall Drives a Stable Landslide to Catastrophic Failure

Alexander L. Handwerger (329-A), Mong-Han Huang (U of Maryland), Eric Fielding (329-A), Adam Booth (Portland State U), and Roland Bürgmann (UC Berkeley)

1. How do fluid pressure perturbations control the behavior of landslides?

- Fluid pressure perturbations from precipitation and snowmelt can trigger landslides.
- Once they occur, some landslides display stable sliding, some display unstable sliding (i.e. catastrophic failure), and some transition from stable to unstable sliding.
- ***Here we seek to understand this transitional behavior.***

2. Study site: The California Coast Ranges

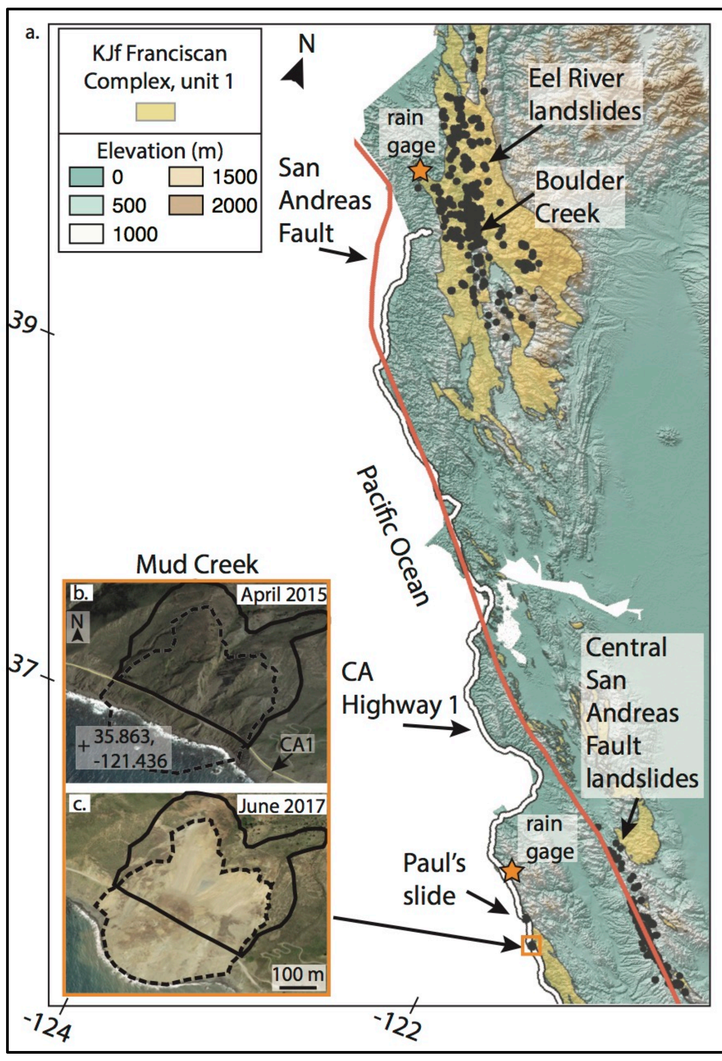

Figure 1. Northern and Central California Coast Ranges. a, Elevation and Franciscan Complex lithologic unit 1 and San Andreas fault[1] draped over a hillshade of the topography. Black polygons show mapped inventories of slow-moving (i.e. stable) landslides[2-5]. **b and c,** Google Earth images of the Mud Creek landslide before and after catastrophic failure. Solid black and dashed black polygons shows pre- and post-catastrophic failure landslide boundaries.

Landslides are pervasive in the California Coast Ranges due to active tectonic uplift, mechanically weak rocks (Franciscan Complex), and high seasonal precipitation.

Precipitation extremes (i.e. dry-to-wet years) are predicted to rise in California over the next several decades due to global warming[6].

- Between 2015 and 2017, California transitioned from a historic drought to extreme rainfall.
- On May 20, 2017, the Mud Creek landslide (Figure 1), located near Big Sur, California failed catastrophically after a prolonged period of heavy rainfall and destroyed California State Highway 1 (CA1). CA1 remains closed at this location.

3. Methods

Satellite and Airborne InSAR

- Radar data provided by ESA Copernicus Sentinel-1 A/B (S1) satellites and NASA Uninhabited Aerial Vehicle Synthetic Aperture Radar (UAVSAR) airplane.
- Radar interferometry (InSAR) is processed with the InSAR Scientific Computing Environment (ISCE) software package developed at JPL/Caltech and Stanford[7].
- We use 3 line-of-sight measurements (2 from S1 and 1 from UAVSAR) to invert for 3D displacements (Figure 2).
- We construct time series inversions with the Generic InSAR Analysis Toolbox[8] (GIAnT; Figure 3).

Pore fluid pressure diffusion model

- We model precipitation-induced changes in pore fluid pressure using a simple 1D linear diffusion equation (Figure 3).

4. Results

- The Mud Creek landslide displayed a minimum of 8 years of stable sliding prior to its catastrophic failure (Figure 2).

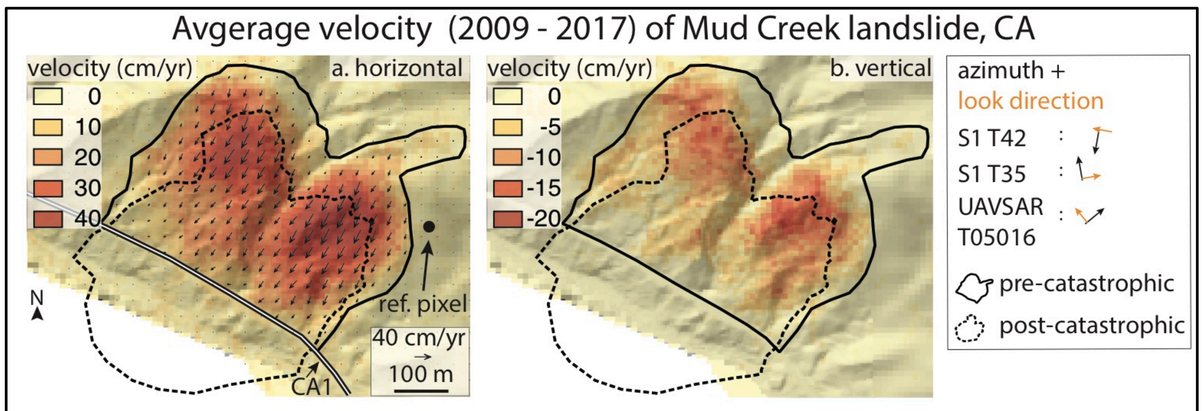

Figure 2. InSAR velocity maps of Mud Creek landslide. a, Average horizontal velocity with velocity vectors draped over a hillshade of the topography. CA1 shown with black and white line. Reference pixel corresponds to a stable area outside the landslide. **b**, Average vertical velocity with negative values indicating downward motion. The azimuth and look direction of the Sentinel-1A/B and UAVSAR instruments are shown with black and orange arrows in the legend. S1 and UAVSAR track numbers are also listed.

- Mud Creek displayed seasonal velocity changes driven by precipitation-induced changes in pore fluid pressure (Figure 3).
- Minimum velocity and pore fluid pressure values occurred during the drought of 2015 and maximum values occurred during the extreme rainfall of 2017.
- Mud Creek displayed a divergence (i.e. second period of acceleration) from its characteristic seasonal velocity patterns leading up to catastrophic failure (see red rectangle in Figure 3).

Figure 3. Velocity, precipitation, and modeled pore-water pressure time series for the Mud Creek landslide. Data is condensed into a single calendar year. The normalized pore pressure is defined as the pore pressure divided by the maximum value over the study period. Water years (WY) are defined as the period between Oct. 1 and Sep. 30.

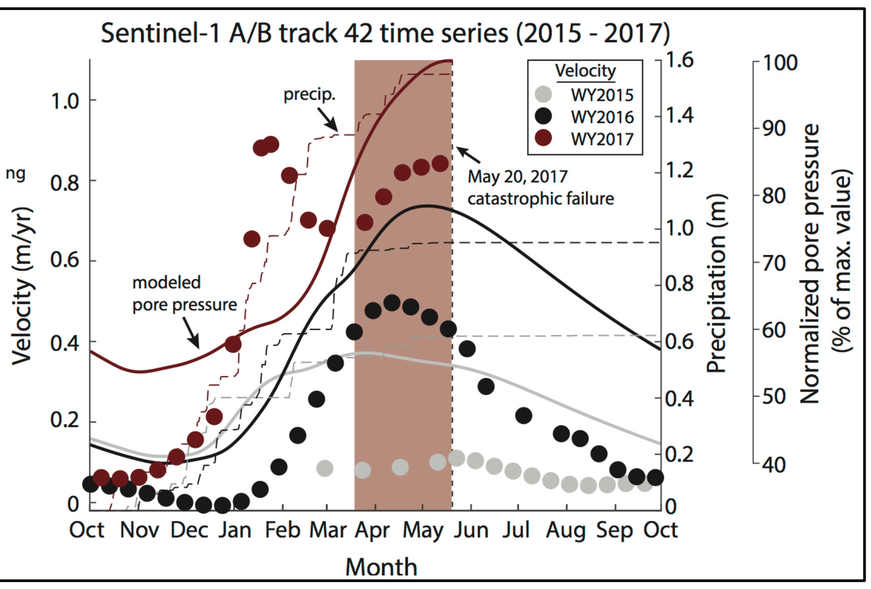

5. Concluding Remarks

- A large increase in pore fluid pressure that occurred during a shift from historic drought to record rainfall triggered a large increase in velocity and overcame the stabilizing mechanisms that had previously inhibited runaway acceleration (i.e. unstable sliding).
- Given the predicted increase in precipitation extremes with a warming climate[6], we hypothesize that there may be an increase the occurrence of landslides in California and we expect it to become more common for landslides to transition from stable to unstable motion.

References:
1. Jennings, C. W., Strand, R. G. & Rogers, T. H. Geologic Map of California: 1969-1973. *Calif. Div. of Mines and Geol.,* (1977).
2. Mackey, B. H. & Roering, J. J. Sediment yield, spatial characteristics, and the long-term evolution of active earthflows determined from airborne lidar and historical aerial photographs, eel river, california. *Geol. Soc. Am. Bull.* **123**, 1560–1576 (2011).
3. Scheingross, J. S. *et al.* Fault-zone controls on the spatial distribution of slow-moving landslides. *Geol. Soc. Am. Bull.* **125**, 473–489 (2013).
4. Handwerger, A. L., Roering, J. J., Schmidt, D. A. & Rempel, A. W. Kinematics of earthflows in the Northern California Coast Ranges using satellite interferometry. *Geomorphology* **246**, 321–333 (2015).
5. Bennett, G. L., Miller, S. R., Roering, J. J. & Schmidt, D. A. Landslides, threshold slopes, and the survival of relict terrain in the wake of the mendocino triple junction. *Geology* **44**, 363–366 (2016).
6. Swain, D. L., Langenbrunner, B., Neelin, J. D. & Hall, A. Increasing precipitation volatility in twenty-first-century california. *Nat. Clim. Chang.* (2018)
7. Rosen, P. A., Gurrola, E., Sacco, G. F. & Zebker, H. The insar scientific computing environment. *Proceedings of the 9th European Conference on Synthetic Aperture Radar*, 730–733 (2012).
8. Agram, P. *et al.* New radar interferometric time series analysis toolbox released. *Eos, Transactions Am. Geophys. Union* **94**, 69–70 (2013).

National Aeronautics and Space Administration
Jet Propulsion Laboratory
California Institute of Technology
Pasadena, California
www.nasa.gov

Poster No. EA-03

National Aeronautics and Space Administration

Investigate Fault Transient Pattern Change and Its Relation to Large Earthquakes

Yingdi Luo (329A) luoyingd@jpl.nasa.gov
Zhen Liu (329A)

I. Introduction

Advances in Geodetic techniques enable us to detect slow earthquake transients (e.g. Slow-Slip Events, SSEs) with improving accuracy and coverage. Recent observations reveal intriguing changes of slow slip transients before or after large earthquakes. However, the physics behind these observations remain largely unknown. How does SSE pattern change during a mega earthquake super-cycle? How do SSEs respond to "external" tectonic perturbations such as stress perturbation from an earthquake, or non-tectonic forces such as tidal modulation and seasonal loading? Can SSE pattern changes shed light on the onset of a large earthquake? To address these questions, we employ laboratory-based rate-and-state friction on subduction zone faults with realistic frictional properties incorporating megathrust earthquake and SSE regions.

II. Observations

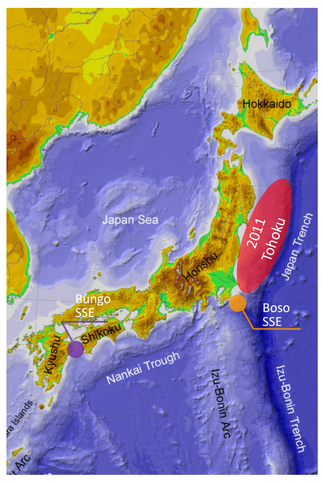

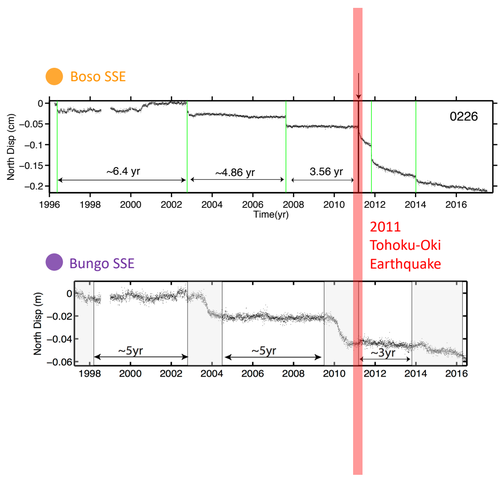

- The remote, long-term SSE in Bungo Channel region occurred after the 2011 Tohoku earthquake was advanced by ~ 2 year and shows different slip distribution.
- The local, Boso SSE has continuously shortening in recurrence interval before the 2011 Tohoku earthquake, and was triggered immediately after the earthquake, next SSE advanced.
- Similar observation in New Zealand and Mexican subduction.

III. Intrinsic SSE Variability

Fault property

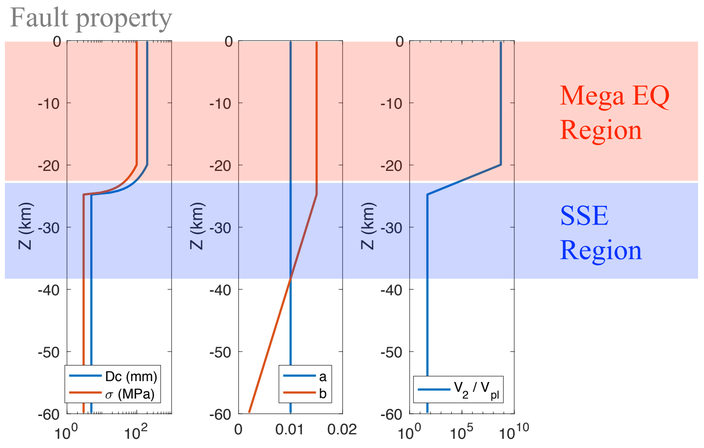

Rate-and-state subduction model
Realistic subduction zone settings:
Megathrust earthquake region
Generating megathrust earthquakes every ~ 1000 years.
SSE region
Generating slow-slip events every ~ 5 years.

The interaction between the SSE region and the megathrust earthquake region naturally forms a "super-cycle" and SSE pattern evolves over different stages of the super-cycle.

SSE – megathrust earthquake super-cycle

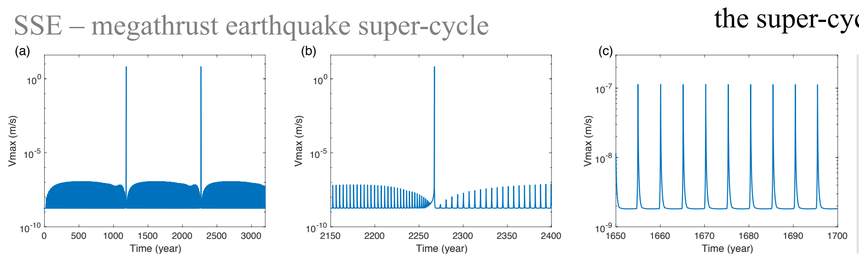

Model results suggests significant SSE pattern change of interval + slip (rate) right before megathrust earthquake: **Observable feature!**

Slip rate of megathrust earthquake and SSE

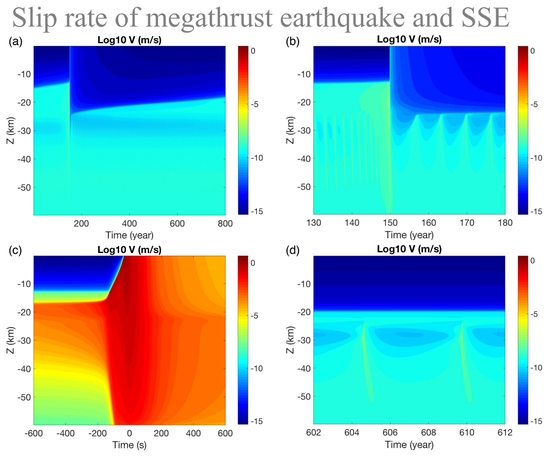

SSE intrinsic variability in super-cycle

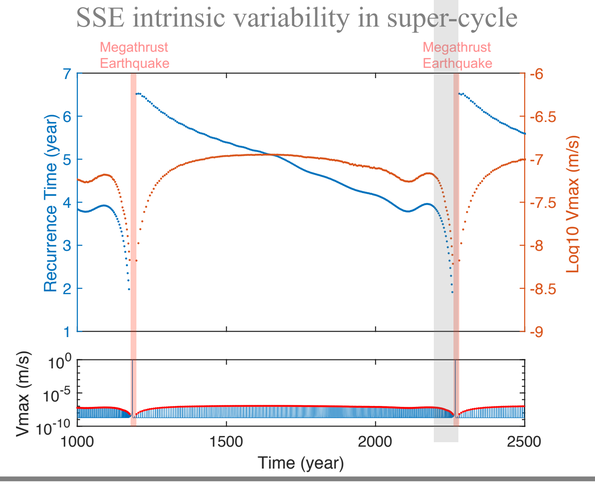

III. SSE Pattern Change Due to External Perturbation

Other than the intrinsic SSE variability due to the interaction of SSE and megathrust earthquake region, SSE pattern may also be affected by external perturbations, e.g. earthquakes.
The effect of such perturbation is approximated by three components:
Co-seismic dynamic perturbation: Gaussian.
co-seismic static perturbation: short-term linear ramp-up.
post-seismic perturbation: long-term linear ramp-up.
Combination of such three components can also approximate other perturbation sources, e.g. tidal modulation, surface loading / unloading, etc.

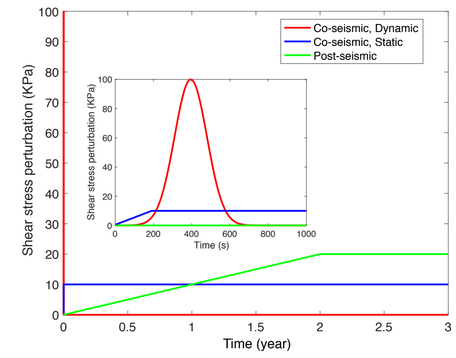

Co-seismic Dynamic Perturbation

Co-seismic dynamic stress perturbations with various amplitude and imposed at different stages of the SSE cycle:

- SSE triggered only at very large (> 200 KPa) amplitude of perturbation.
- Next SSE delayed.

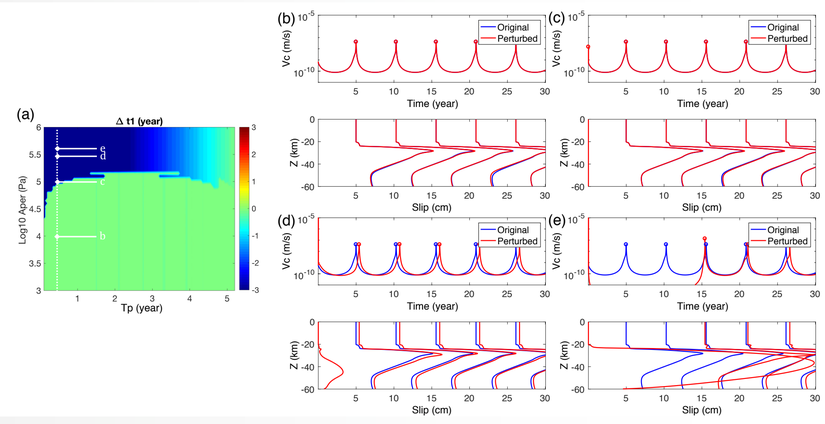

Co-seismic Static Perturbation

Co-seismic static stress perturbations with various amplitude and imposed at different stages of the SSE cycle:

- SSEs will be advanced with co-seismic static stress perturbation.
- The amount of advancing in general is roughly proportional to the perturbation amplitude.
- A ~ 6 KPa co-seismic static perturbation is sufficient to advance the next SSE by ~ 1.3 years.
- Large (> 20 KPa) co-seismic static perturbation can triggered the next SSE (almost) immediately.

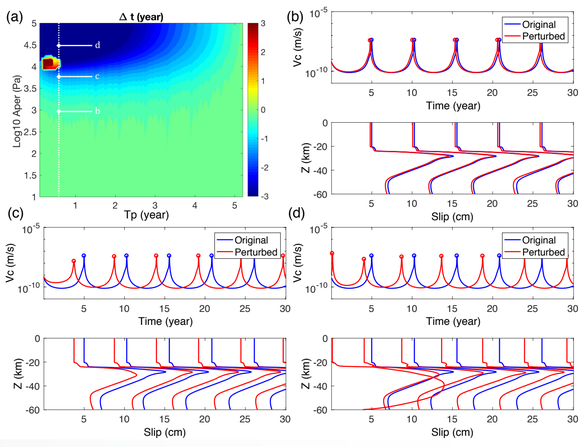

Post-seismic Perturbation

Post-seismic stress perturbations with various amplitude and duration:

- SSEs advanced.
- Amount of advancing proportional to amplitude.
- A ~ 10 KPa advance the next SSE by ~ 2 years.
- Long-duration perturbation affect multiple SSEs.

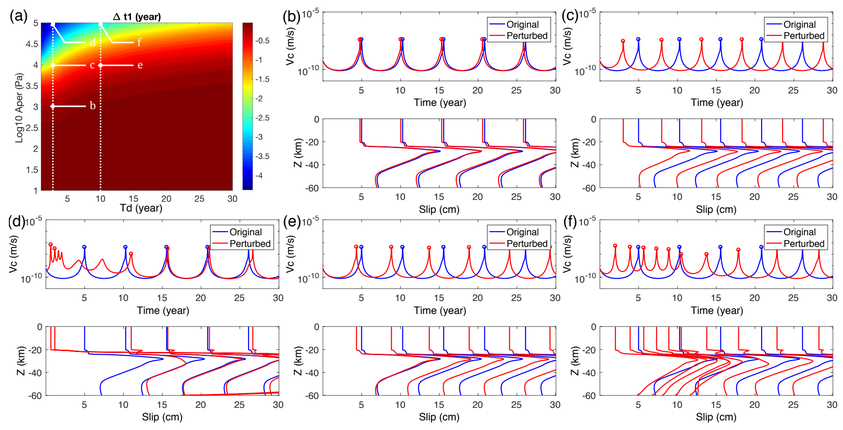

IV. Conclusions

"Intrinsic variability": The interaction between the SSE region and the megathrust region will cause intrinsic variabilities to the SSE pattern, which changes the slip pattern and recurrence intervals during the entire course of the megathrust super-cycle. More importantly, in the last several cycles of SSE right before the next megathrust earthquake (tens of years in our simulation case), the SSE recurrence intervals will rapidly decrease, accompanied by a rapid decrease of SSE peak slip rate (and slip) simultaneously.
"External effect": The modeled SSE pattern changes in response to the co-seismic and post-seismic stress perturbation suggest that even a remote earthquake can significantly change the spatiotemporal pattern of SSEs due to the low stress-drop nature of SSE and its proneness to stress perturbations.

National Aeronautics and Space Administration
Jet Propulsion Laboratory
California Institute of Technology
Pasadena, California

www.nasa.gov

Selected References:

Kato, A., Igarashi, T., & Obara, K. (2014). Detection of a hidden Boso slow slip event immediately after the 2011 Mw 9.0 Tohoku-Oki earthquake, Japan. Geophysical Research Letters, 41(16), 5868-5874.
Luo, Y., Ampuero, J. P., Galvez, P., Van den Ende, M., & Idini, B. (2017). QDYN: A Quasi-DYNamic Earthquake Simulator (V1.1). DOI: :10.5281/zenodo.322459
Luo, Y., & Ampuero, J. P. (2018). Stability of faults with heterogeneous friction properties and effective normal stress. Tectonophysics, 733, 257-272 pp.
Luo, Y., & Liu, Z. Slow-Slip recurrent pattern changes: perturbation responding and possible scenarios of precursor towards a megathrust earthquake. In prep
Matsuzawa, T., Shibazaki, B., Obara, K., & Hirose, H. (2013). Comprehensive model of short-and long-term slow slip events in the Shikoku region of Japan, incorporating a realistic plate configuration. Geophysical Research Letters, 40(19), 5125-5130.

QDYN

https://github.com/ydluo/qdyn

Poster No. EA-04

National Aeronautics and Space Administration

Weighing Hurricane Harvey's Floodwaters Using GPS Data

Author: Chris Milliner (329A)

Kathryn Materna (UC Berkeley), Roland Bürgmann (UC Berkeley), Yuning Fu (Bowling Green),
Angelyn Moore (335N), David Bekaert (334H), Surendra Adhikari (329A), Donald Argus (335N)

1. Introduction

Hurricane Harvey made landfall in south Texas lasting seven days and deposited 103 km^3 of water as it migrated across the Gulf coast.

Question During a hurricane we can measure precipitation (below), however, what happens to that water once deposited? **Can we track terrestrial water storage and its dissipation following a major hurricane?** This is important for monitoring the extent of flooding, estimating recovery time of the drainage system and accuratley forecasting downstream river levels.

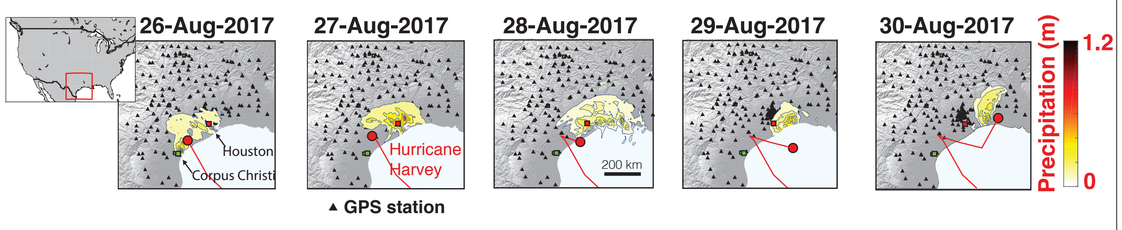

Objective Our objective is to constrain daily changes in water storage deposited by Hurricane Harvey by using GPS data that measures solid Earth's elastic response to water loading.

Daily estimates of flood extent is challenging, GRACE has monthly and 300 km resolution (too coarse), optical and radar image aquistion can take days and can't measrue water depth, while field surveys are point estimates that are spatially limited.

2. Methods

Land Subsidence From Water Loading

Below left, forward model, $\boldsymbol{Gm = d}$. Loading of Earth's elastic crust from a disk of water (of unknown thickness m) causes land subsidence, which can be measured using GPS ($\boldsymbol{d}$). These data can be inverted to estimate water volume.

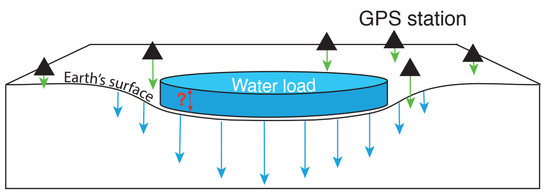

$$\begin{bmatrix} WG_v \\ WG_u \\ WG_u \\ \lambda S \\ \beta U \end{bmatrix} [m_t] = \begin{bmatrix} Wd_t^v \\ Wd_t^e \\ Wd_t^n \\ 0 \\ \beta U m_{t-1} \end{bmatrix}$$

d = data, v = vertical, e = east, n = north
G = Greens function's
m = water thickness on day (t)

GPS Filtering - Independent Component Analysis (ICA)

➢ The vertical component of GPS is particularly noisy due to the suboptimal satellite geometry relative to receiver, antenna phase center variations and atmospheric corrections. To resolve this we use independent component analysis (ICA), a statistical feature extraction technique, to remove common-mode error (systematic bias) and extract the hydrologic signal.

➢ GPS positions are processed using JPL's GIPSY-OASIS II software.

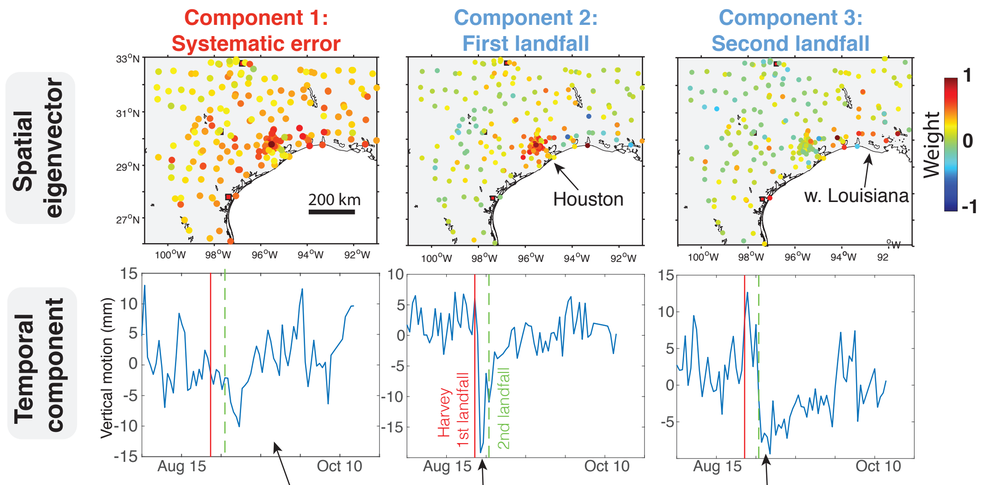

First component exhibits near-uniform spatial motion (top), with no clear deviation in positions during arrival of Harvey (red line). **This component reflects common-mode error and is removed.**

This component indicates stations around Houston (top) exhibit marked **subsidence during initial landfall** of Harvey (bottom).

Third component indicates stations around west Louisiana (top) exhibit marked **subsidence during second landfall** of Harvey (bottom)

Filtered GPS timeseries

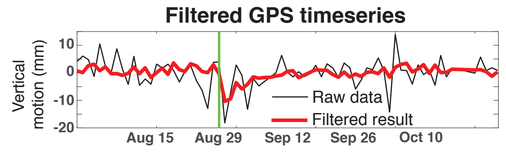

An example of a filtered vertical position timeseries from a GPS station in Houston. Recombining the 2nd and 3rd components from above removes systematic bias, extracts the hydrologic signal, and removes motions local to the GPS station

3. Results

Filtered GPS Data (d)

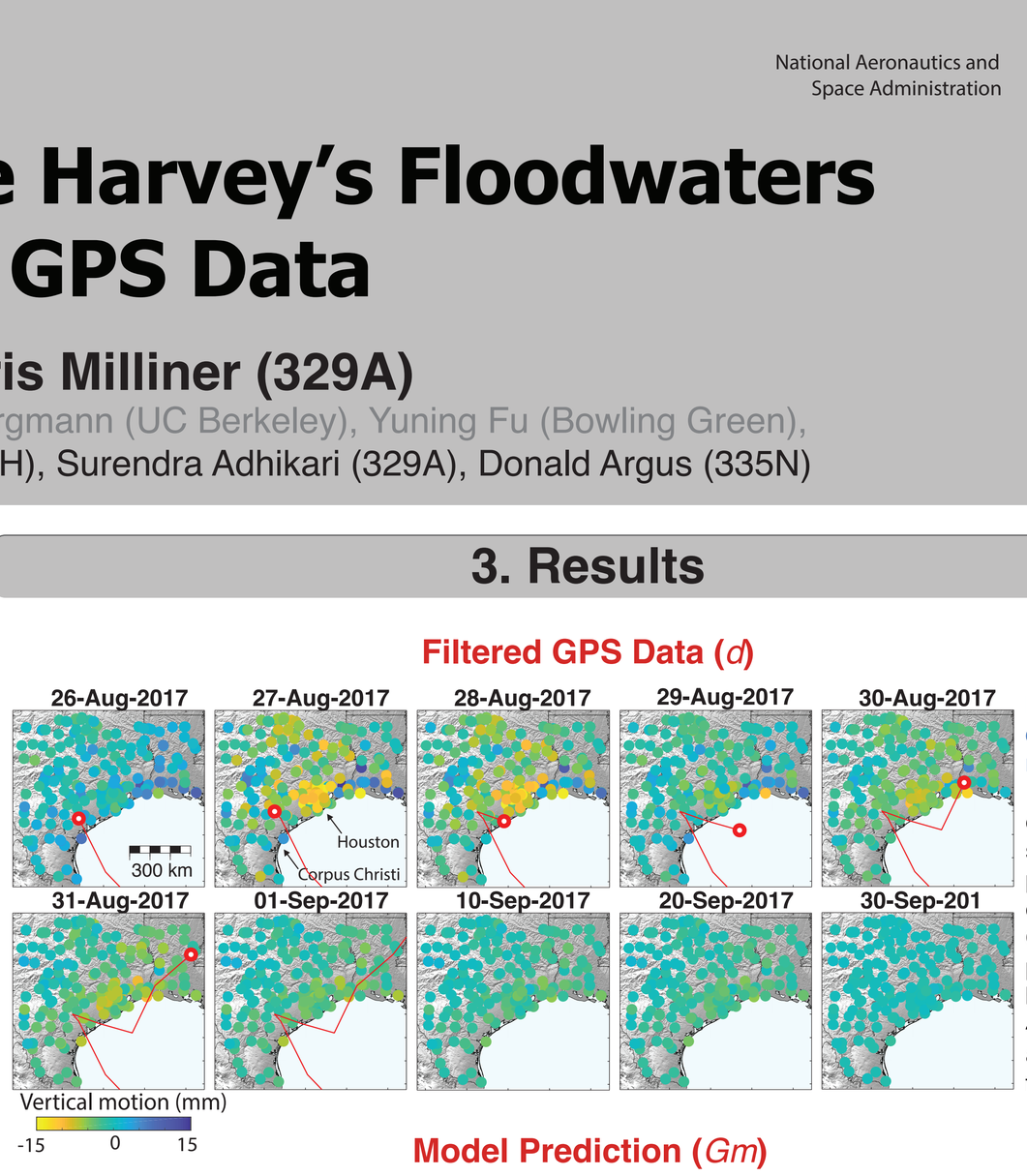

Filtered GPS motions each day during arrival of Hurricane Harvey. GPS subsidence (yellow) corresponds closley with position of Harvey's eye (red dot) across Gulf coast over 7 day period. This is followed by gradual uplift over ~5 weeks. These data are inverted to estimatre water storage.

Model Prediction (Gm)

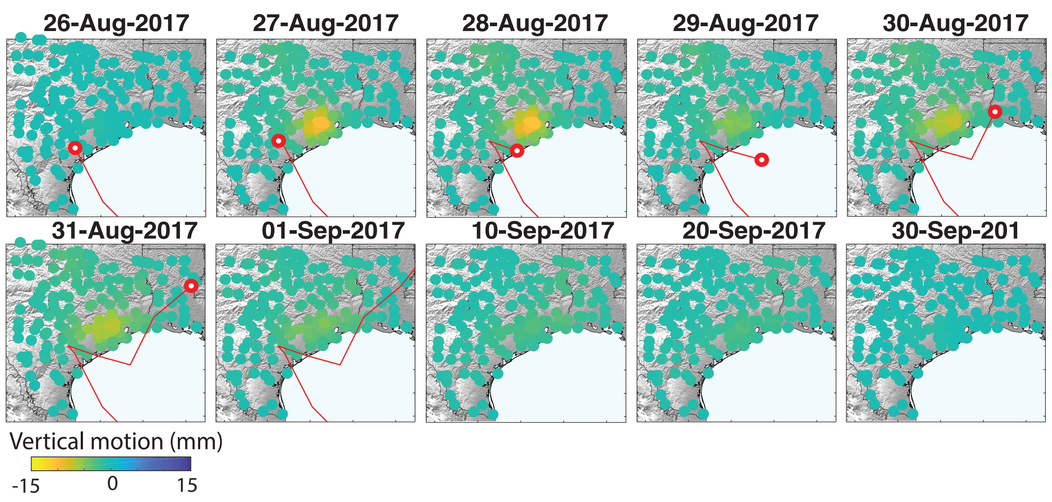

Forward result (left) from our best model (shown below). Our model predicts subsidence around Houston that corresponds with migrating position of Harvey, followed by gradual uplift indicating water dissipatation.

Inversion Result: Daily Estimate of Water Storage

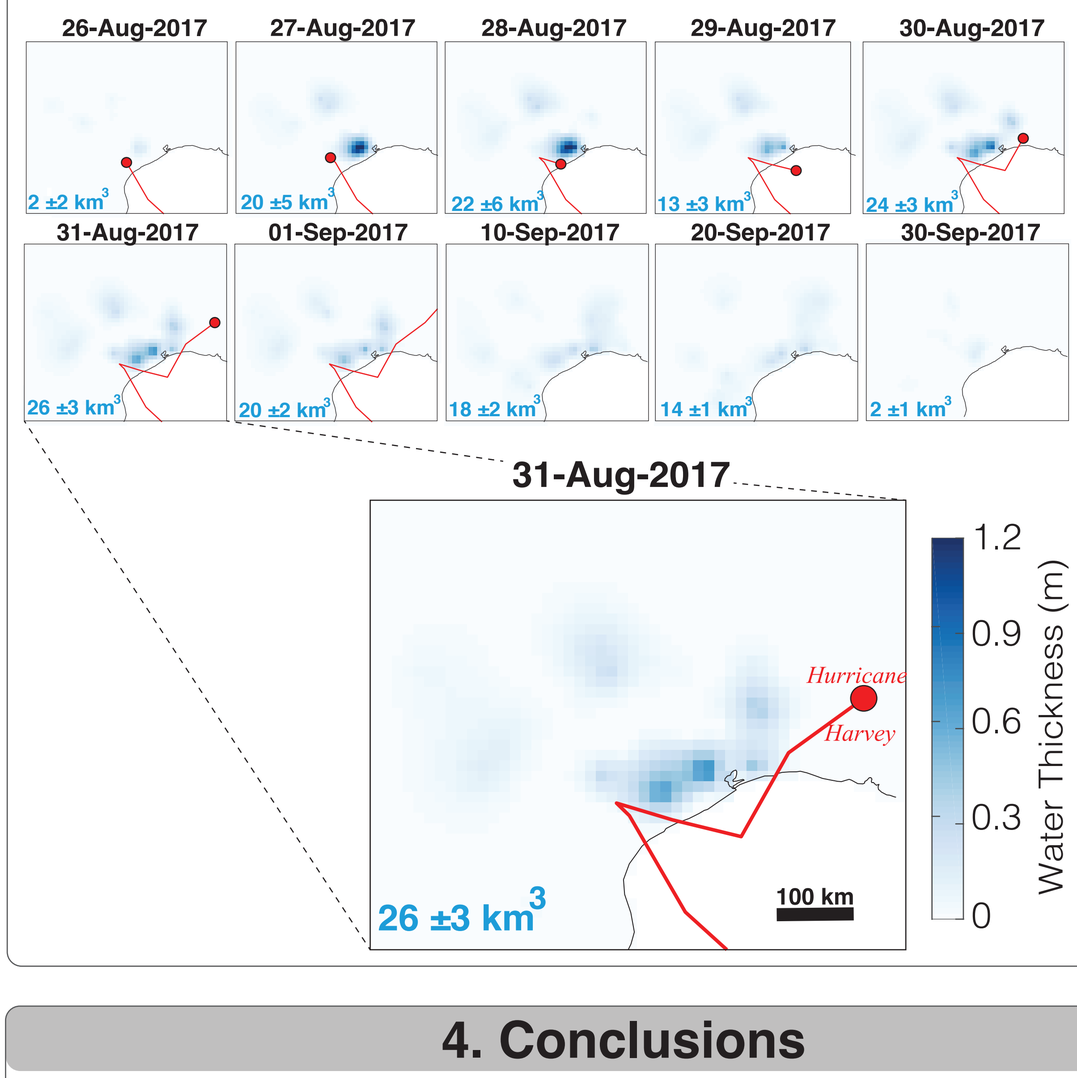

Left, evolution of water storage estimated from inverting data above. Model values (blue) show estimated thickness of water disk (Fig. 2), providing total water volume each day (lower left value).

4. Conclusions

➢ We demonstrate continuous GPS data can track daily changes of water storage during and following a major hurricane, suggesting a new role for GPS as a flood monitoring system.

➢ Inverting GPS data shows one-third of Harvey's total water was captured and retained on land, taking 5 weeks to dissipate at a rate of 1 gigaton/day.

➢ Water extent constrained from GPS can be applied to future hurricane events, that can help improve opertaional flood forecasts of downstream river and dam levels used by flood managers, and help fill in data gaps of GRACE which has montly resolution.

At time of writing this study was in review in Science Advances

Poster No. EA-05

National Aeronautics and Space Administration
Jet Propulsion Laboratory
California Institute of Technology
Pasadena, California
www.nasa.gov

National Aeronautics and Space Administration

Bayesian statistics of Glacial Isostatic Adjustment for GRACE and sea level

Author: Lambert Caron (329-C)
Erik Ivins, Eric Larour and Surendra Adhikari (329-C)

Abstract

We provide a new analysis of glacial isostatic adjustment (GIA) with the goal of assembling the model uncertainty statistics required for rigorously extracting trends in surface mass from the Gravity Recovery and Climate Experiment (GRACE) mission.
Such statistics are essential for deciphering sea level, ocean mass, and hydrological changes because the latter signals can be relatively small (<2 mm/yr water height equivalent) over very large regions, such as major ocean basins and watersheds.
With abundant new >7 year continuous measurements of vertical land motion (VLM) reported by Global Positioning System stations on bedrock and new relative sea level records, our new statistical evaluation of GIA uncertainties incorporates Bayesian methodologies.
A unique aspect of the method is that both the ice history and 1-D Earth structure vary through a total of 128,000 forward models. We find that best fit models poorly capture the statistical inferences needed to correctly invert for lower mantle viscosity and that GIA uncertainty exceeds the uncertainty ascribed to trends from 14 years of GRACE data in polar regions.

What is GIA?

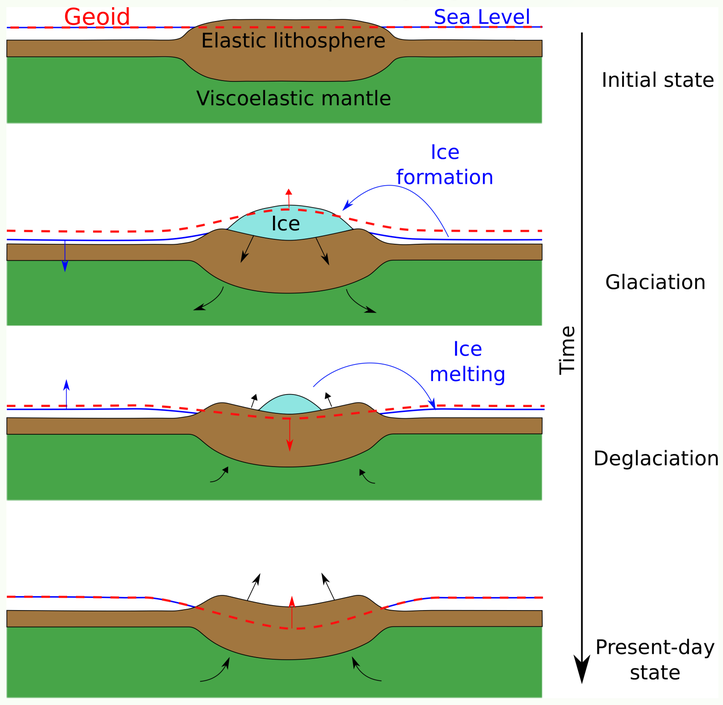

Data constraints

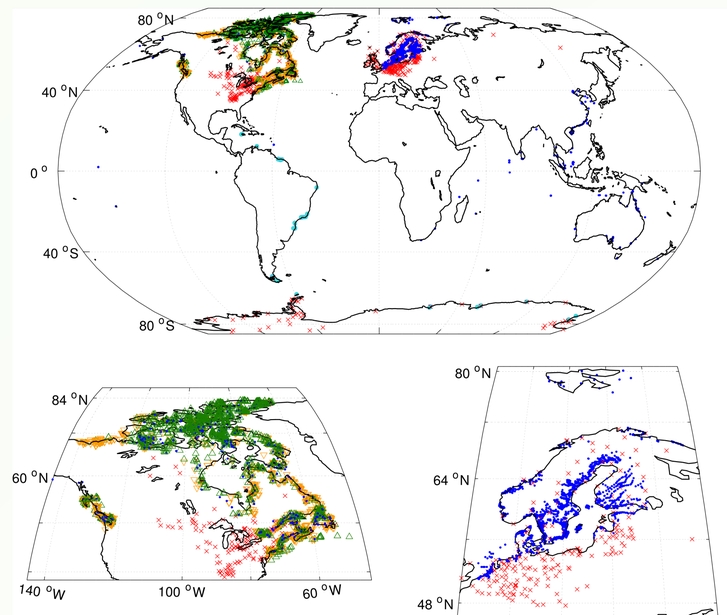

Red: Vertical GPS velocities
Rest: Relative Sea Level indicators (up to 35kyr old)

Parameters explored:

Earth rheology

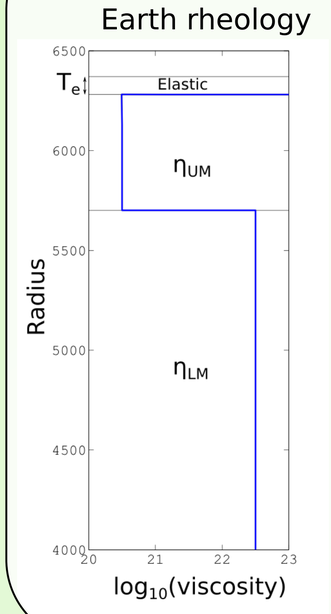

Ice history

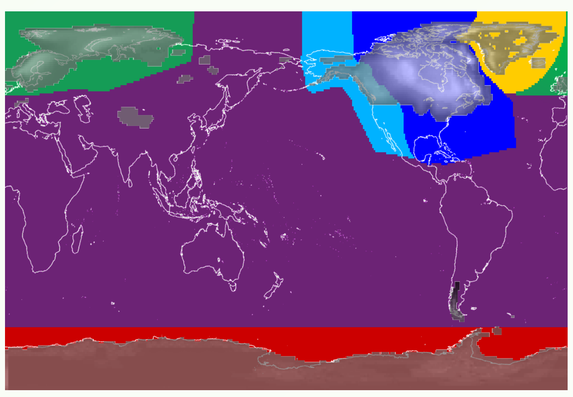

Scaling a reference ice model (shades of grey, combination of ANU and IJ05) by regional coefficients (colors).

Probabilistic approach to GIA:

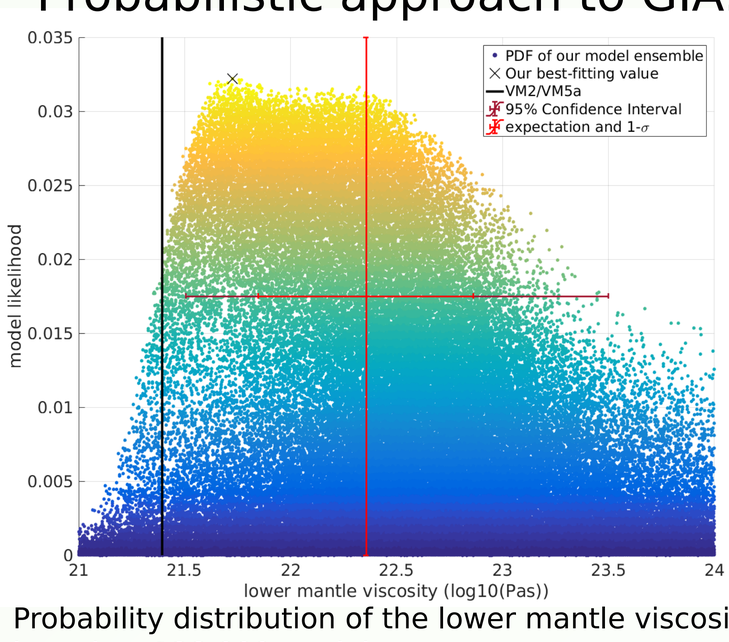

Probability distribution of the lower mantle viscosity based on 128,000 model runs.

Take home messages

- We can calculate formal GIA statistics, including uncertainty.

- The classic "best-fit" approach leads to biased lower mantle viscosity, and thus long wavelength GIA.

- Bigger uncertainty in mass changes than GRACE's in polar regions.
At the global scale, it represents about twice what had been speculated before.

- Check out our GRL publication "GIA Model Statistics for GRACE Hydrology, Cryosphere and Ocean Science", DOI: 10.1002/2017GL076644.
Download our results at:
http://vesl.jpl.nasa.gov/solid-earth/gia

Present-day predictions and uncertainty:

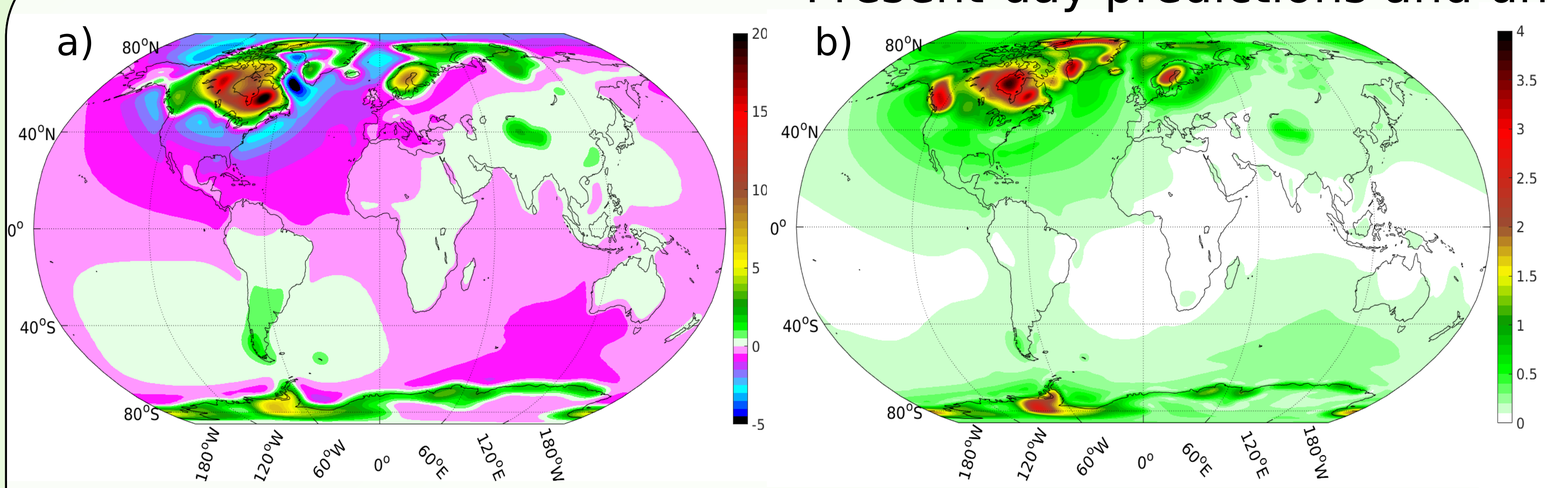

Vertical Land Motion (mm/yr): **a)** expectation, **b)** uncertainty

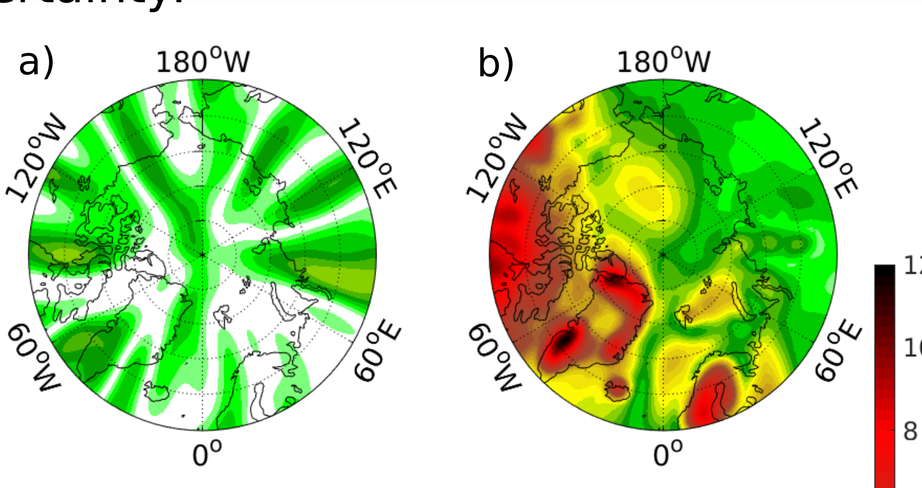

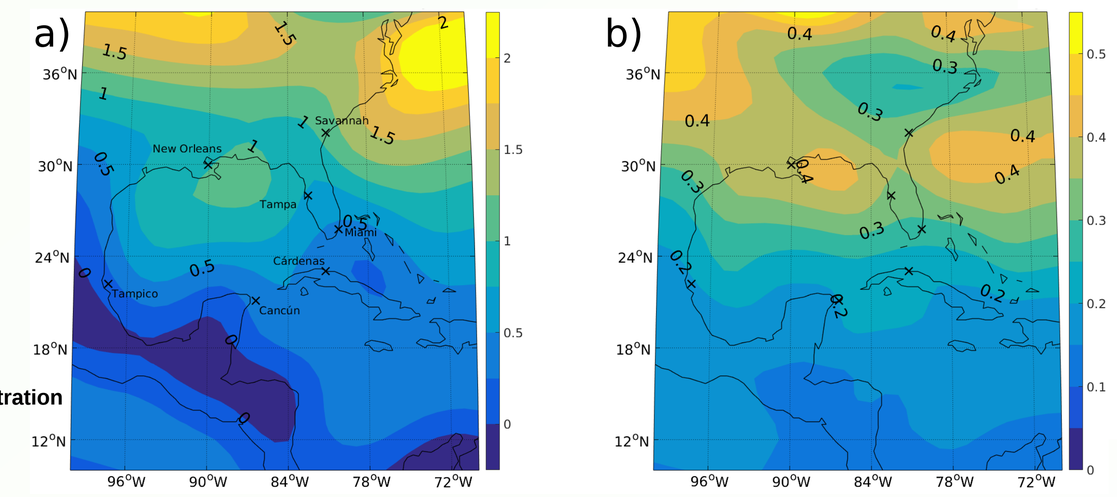

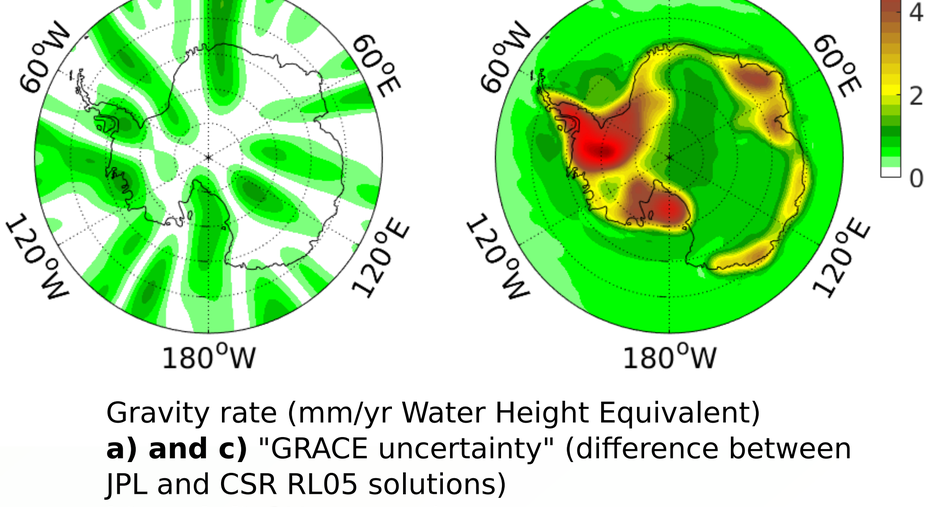

Relative sea level rate (mm/yr): **a)** expectation, **b)** uncertainty

Gravity rate (mm/yr Water Height Equivalent)
a) and c) "GRACE uncertainty" (difference between JPL and CSR RL05 solutions)
b) and d) GIA uncertainty

National Aeronautics and Space Administration
Jet Propulsion Laboratory
California Institute of Technology
Pasadena, California

www.nasa.gov

Poster No. EA-06

National Aeronautics and Space Administration

Introducing a gridded wildfire risk model using NASA Satellite Observations in the United States

Author: Alireza Farahmand (329E)

JT Reager (329F), Natasha Stavros (398P), Ali Behrangi (329E), James Randerson[1]

[1] University of California, Irvine

Introduction

Fires are a key disturbance globally acting as a catalyst for terrestrial ecosystem change and contributing significantly to both carbon emissions and changes in surface albedo. The socioeconomic impacts of wildfire activities are also significant with wildfire activity results in billions of dollars of losses every year. Numerous studies have aimed to predict the likelihood of fire danger, but few studies use remote sensing data to map fire danger at scales commensurate with regional management decisions (e.g., deployment of resources nationally throughout fire season with seasonal and monthly prediction). Here, we use NASA Gravity Recovery And Climate Experiment (GRACE) assimilated surface soil moisture, NASA Atmospheric Infrared Sounder (AIRS) vapor pressure deficit, MODIS Enhanced Vegetation Index (EVI) and landcover products, along with US Forest Service historical fire activity data to generate probabilistic monthly fire potential maps in the United States. These maps can be useful in not only government operational allocation of fire management resources, but also improving understanding of the Earth System and how it is changing in order to refine predictions of fire extremes.

Datasets

- GRACE (Gravity Recovery and Climate Experiment)-assimilated SM (Soil Moisture)
- AIRS (Atmospheric infrared sounder) Vapor Pressure Deficit (VPD)
- MODIS (Moderate Resolution Imaging Spectroradiometer) EVI (Enhanced Vegetation Index)
- Wildfire burned area from USDA (United States Department of Agriculture) Forest Service's Fire Program Analysis Fire-occurance database (FPA FOD)
- USGS (United States Geological Survey) National land-cover databse
- Spatial Resolution: 0.25 degree
- Temporal Resolution: Monthly
- Data Length: 2004-2013

Methodology

- Derive SM, VPD, EVI relationship with fire burned area in land cover types deciduous, evergreen, shrub land, herbaceous, and wetland
- Divide the hydrologic variable range into 10 bins
- Calculate fire burned area:

$$Forecast\ Buned\ Area = \frac{Sum\ brned\ area\ in\ each\ bin}{total\ number\ o\ samples\ in\ each\ bin}$$

- Pick the hydrologic variable with highest correlation to the fire data

One look-up table is generated for each land-cover type. Once a real-time observation becomes available, the corresponding look-up table will be utilized to predict the likelihood of fire occurrence. Figure 2 shows look-up tables generated for land-cover type shrubland using 2-month lead EVI observations. EVI shows highest correlations to the fire data in this land-cover type.

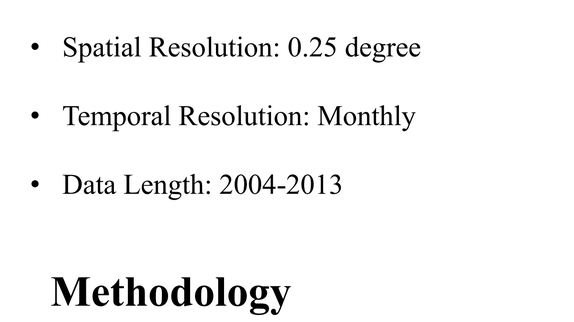

Figure 1:MODIS land-cover map

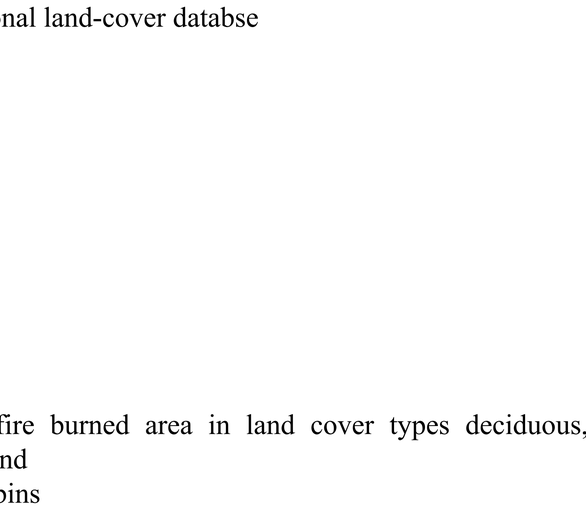

Figure 2: Model Development for Shrubland

Results

- Use the developed algorithm to predict burned area for the 2004-2013 period
- Derive the residuals by removing the climatology from the prediction and observation values. Figure 3a and 3b are the residuals of observations and predictions for August 2013 respectively
- The residuals are adjusted by empirically deriving the probability of residuals in each land-cover type. The Gringorton empirical probability is used to derive the probabilities:

$$p(x_i) = \frac{i - 0.44}{n + 12}$$

Where i is the rank of residuals data (observation or predictions) from the smallest (for each land-cover type) , and n is the sample size. Figure 3c and 3d are the probabilities of observation and prediction residuals in August 2013.

- To validate the model, we calculate the RMSE (Root Mean Squared Error) of probabilities of observations and predictions. This is performed via:

$$RMSE = \sqrt{\frac{\sum_{i=1}^{n}(X_{obs,i} - X_{model,})^2}{n}}$$

where X_{obs} is observed values and X_{model} is predicted values at time/place i. Figure 3e is RMSE for August 2013. Figure 3f is the time-series of RMSE for the 2004-2013 period.

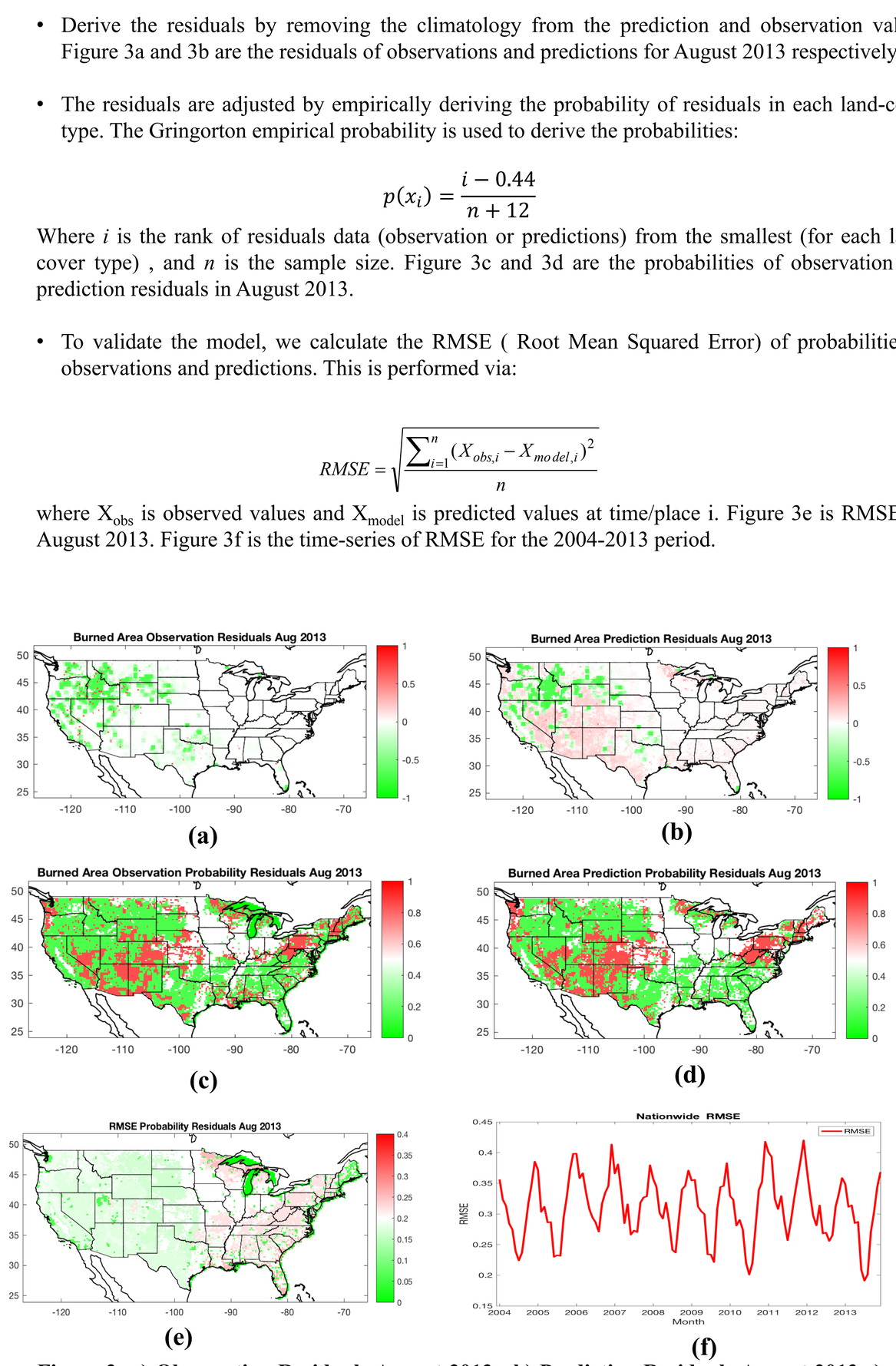

Figure 3: a) Observation Residuals August 2013 ; b) Prediction Residuals August 2013 c) Observation Probability of Residuals August 2013 d) Prediction Probability of Residuals August 2013 e) RMSE August 2013 f) Time series of RMSE 2004-2013

Conclusion

- This study used VPD, SM and EVI to predict the likelihood of monthly fire occurrences across the US.
- We have validated the model across various landcover and GACC types. The result show that the model can potentially predict the likelihood of fire occurrences with relatively small margin of errors.
- These maps can be useful in not only government operational allocation of fire management resources, but also improving understanding of the Earth System and how it is changing in order to refine predictions of fire extremes

National Aeronautics and Space Administration

Jet Propulsion Laboratory
California Institute of Technology
Pasadena, California

www.nasa.gov

Poster No. EA-08

National Aeronautics and Space Administration

Improving discharge estimates of the RAPID river routing model with data assimilation

Author: Charlotte M. Emery (329F)

Cedric H. David (329F), Mike Turmon (398L), Jonathan M. Hobbs (398L), John T. Reager (329F), James S. Famiglietti (329F)

INTRODUCTION

RAPID (David et al., 2011) is a routing model based on the Muskingum method that is capable of estimating river streamflow over large scales with a relatively short computing time. This model only requires limited inputs: a reach-based river network, and lateral surface and subsurface flow into the rivers. The relatively simple model physics imply that RAPID simulations could be significantly improved by including a data assimilation capability. Here we present the developments of such data assimilation approach into RAPID. Given the linear and matrix-based structure of the model, we chose to apply a direct Kalman filter, hence allowing for the preservation of high computational speed. We correct the simulated streamflow by assimilating streamflow observations and correcting the lateral runoff. Our results demonstrate the feasibility of the approach and show promise for our ability to assimilate SWOT river observations globally once the mission is in operation. This work is supported by JPL's Western States Water Mission as well as NASA's SWOT Science Team.

RAPID RIVER MODEL

RAPID (Routing Application for Parallel Computation of Discharges, David et al., 2011) is a **river routing model** based on the Muskingum method.

The river catchment is modeled as a **network of reaches N**. A reach has only **one downstream** reach but can have **several upstream reaches**. The 1D Muskingum method is adapted to the multidimensional network:

$$(\mathbf{I}-\mathbf{C_1N})\mathbf{Q}(t+1) = (\mathbf{C_1}+\mathbf{C_2})\mathbf{Q^e}(t)+(\mathbf{C_3}+\mathbf{C_2N})\mathbf{Q}(t)$$

For any reach, the updated streamflow is a function the surface/subsurface lateral inflow $\mathbf{Q^e}$ from a Land Surface Model, the streamflow $\mathbf{Q}$, and the streamflow from upstream reaches $\mathbf{NQ}$.

The routing model is **parallelized** and optimized to **run rapidly with a minimal computational cost** over large domains.

DATA ASSIMILATION METHOD

RAPID uses **linear algebra** and so we use the simple **Kalman Filter** to maintain computational efficiency.

We assimilate **daily-averaged** in situ **discharge** measurements to correct the lateral runoff model input. The lateral runoff is available **every 3 hours** so we decided to **correct the runoff daily-mean** based on the day 8 runoff entries (Figure 1).

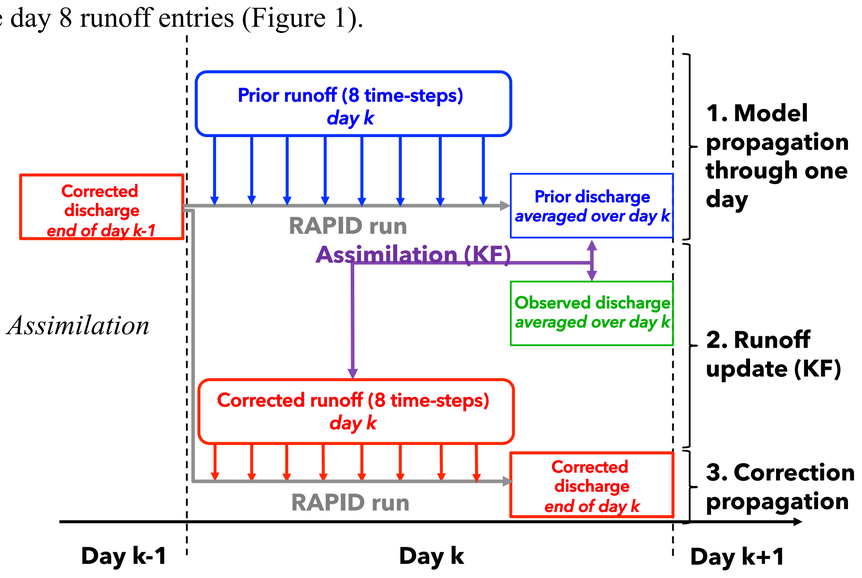

Figure 1: Assimilation scheme

RUNOFF ERROR MODEL

NLDAS VIC runoff is used as **forcing for RAPID** and will be **updated through data assimilation**. For the KF, the runoff error need to be estimated.

NLDAS also provides runoff from **two other models** (MOSAIC and NOAH). The **mean runoff over the three available models** (VIC+MOSAIC+NOAH) is assumed to be the **"true" runoff**.

The runoff error statistics is therefore estimated from the **deviation of the VIC runoff from the "true" runoff**.

RESULTS OVER THE GUADALUPE AND SAN ANTONIO RIVER BASINS (TX)

Data assimilation results for **6 months of simulations from Jan 1st, 2004** (Figure 2) over the Guadalupe and San-Antonio river catchments in Texas. Among all **36 in situ gauges available**, **21 were assimilated** (circles markers) and the **15 remaining were kept for validation** (square markers).

Figure 2: Assimilation results

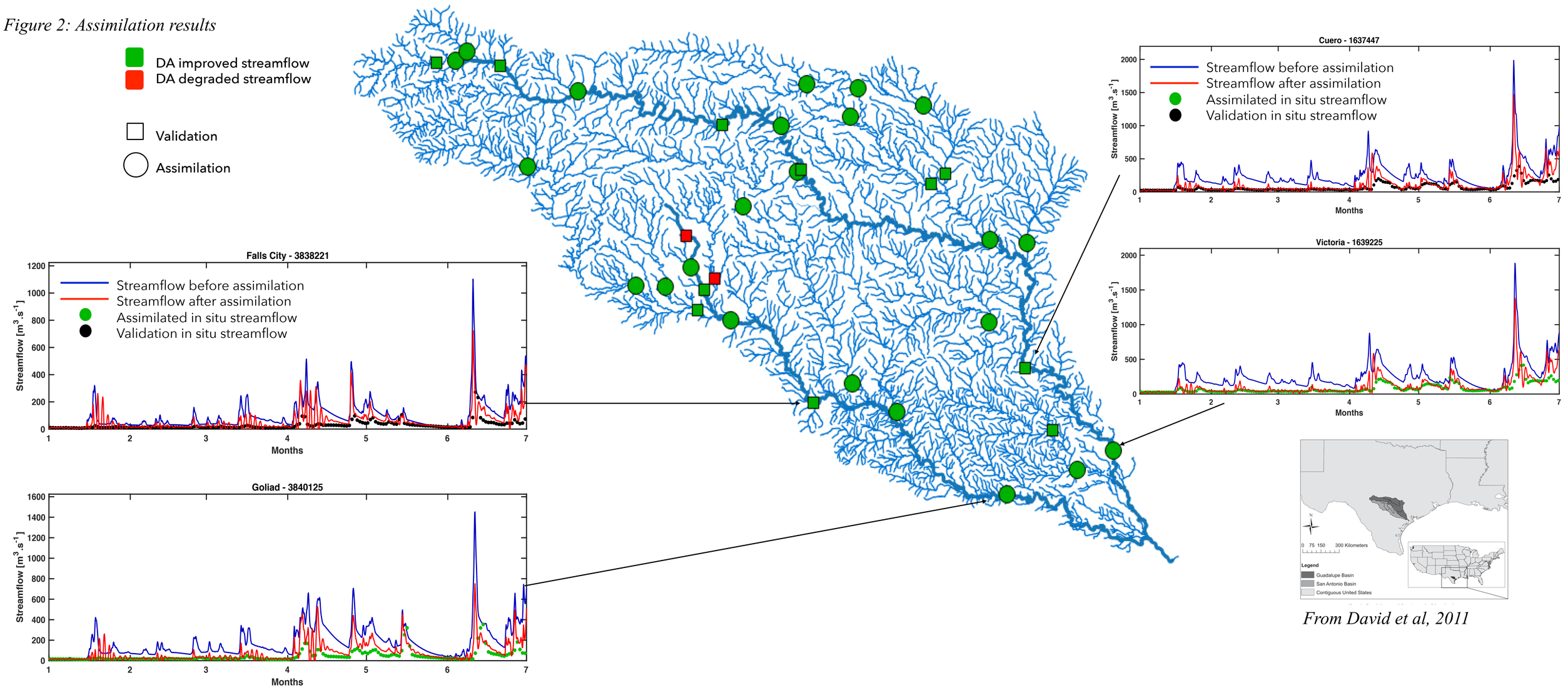

From David et al, 2011

CONCLUSIONS & PERSPECTIVES

- Our method leads to improved simulations with an overall increase of the Nash-Sutcliffe efficiency.
- Future work is required to apply the method over larger continental/global scale domain (e.g. Western States of the United States)
- Method could also be applied to remotely-sensed data (e.g. Jason and/or SWOT altimetry measurements)

National Aeronautics and Space Administration

Jet Propulsion Laboratory
California Institute of Technology
Pasadena, California

REFERENCES

- **David et al, 2011**, *River Network Routing on the NHDPlus Dataset*, 2011, Journal of Hydrometeorology, 12, 913-934
- **National Land Data Assimilation System (NLDAS):** https://ldas.gsfc.nasa.gov/index.php
- **Emery et al, 20xx**, in preparation

www.nasa.gov

Poster No. EA-10

National Aeronautics and Space Administration

Predicting Groundwater Depletion in the Central Valley, CA

Elias C. Massoud* (Jet Propulsion Laboratory, California Institute of Technology – Section 329F)
Adam J. Purdy (Jet Propulsion Laboratory, California Institute of Technology – Section 329G)
James S. Famiglietti (Jet Propulsion Laboratory, California Institute of Technology – Section 329F)

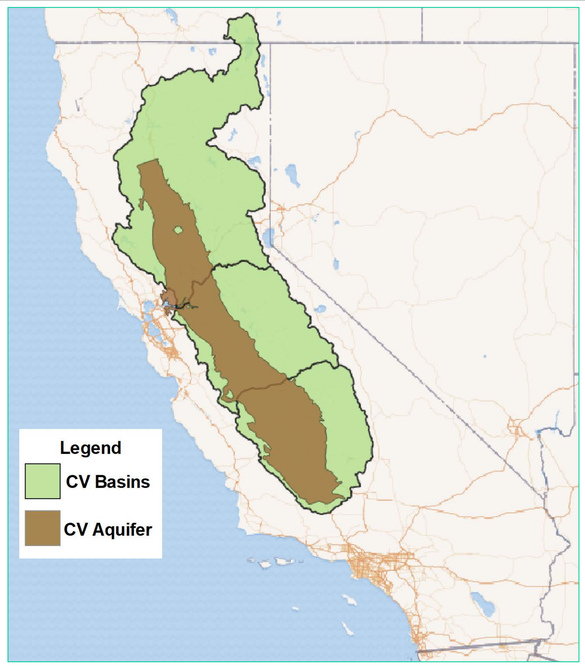

California's groundwater resources are depleting. Accurate knowledge of California's groundwater is of paramount importance to sustain a multi-billion-dollar agriculture industry during prolonged droughts. In this study, we develop a groundwater storage model for California's Central Valley using supply and demand information from the state. The model is then used to predict future changes in groundwater storage from downscaled climate projections.

Fig.1 (Left) The green basin boundary is the area used to downscale the precipitation projections. The brown boundary indicates regions where the aggregated groundwater storage changes are represented in this study.

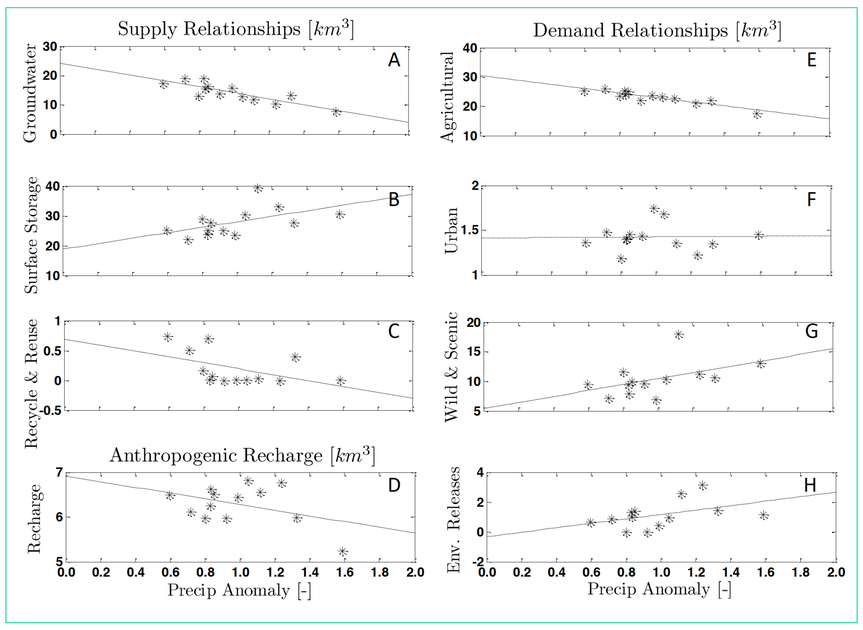

Fig.2 (Left)
Empirical relationships showing Department of Water Resources supply and demand variables with precipitation.

This figure indicates how a given variable responds to precipitation each year. For example, agricultural demand is greater during dry years or surface water supplies are higher during wet years.

Fig.3 (Right)
Schematic representing conceptualized model structure.
PP represents precipitation anomalies each year.

Fig.4 (Bottom)
Butterfly chart obtained by driving the model with future precipitation. These estimates are fresh water demands during each year and the respective fresh water supplies of each year.

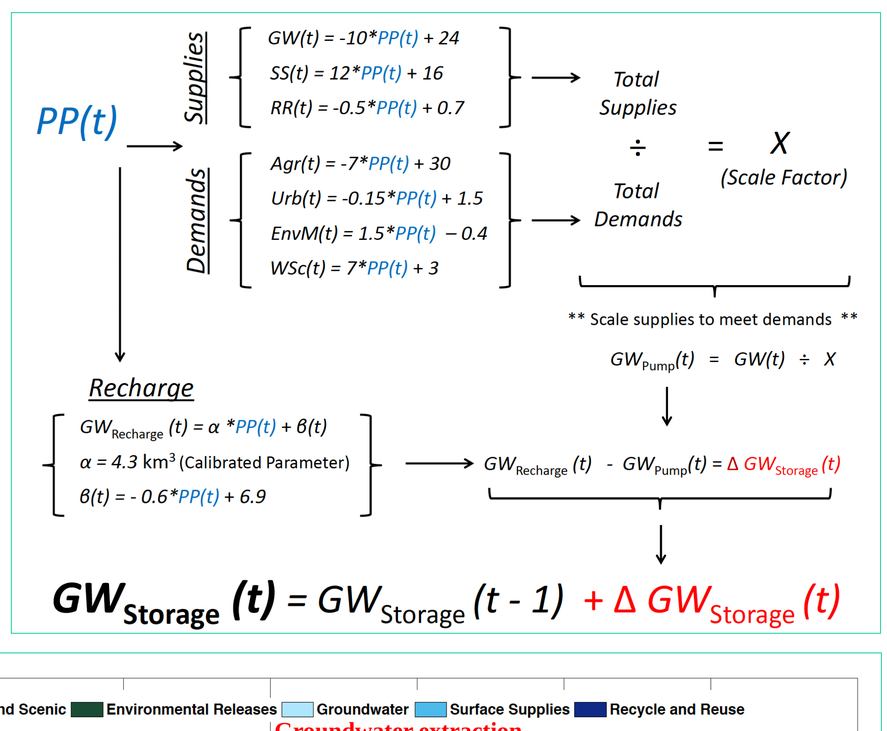

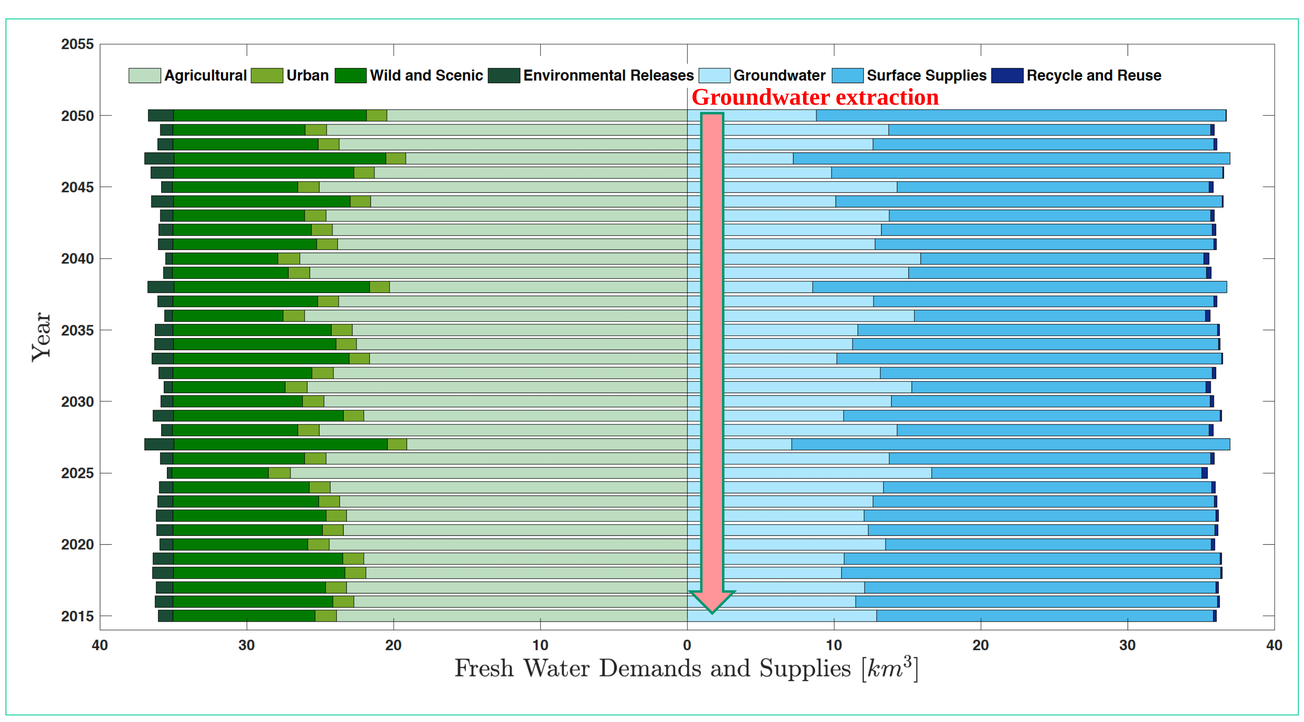

Fig.5 (Bottom) The model is evaluated against 34 years of historic estimates of changes in groundwater storage derived from the United States Geological Survey's Central Valley Hydrologic Model (USGS CVHM) and NASA's Gravity Recovery and Climate Experiment (NASA GRACE) satellites. Yearly precipitation anomalies are shown in Panel A. Model Simulations in Panel B. Observed data in Panel C.

Fig.6 (Bottom) The calibrated model is used to predict future changes in groundwater storage under various precipitation scenarios. All simulations support the need for collective statewide management to prevent continued depletion of groundwater availability.

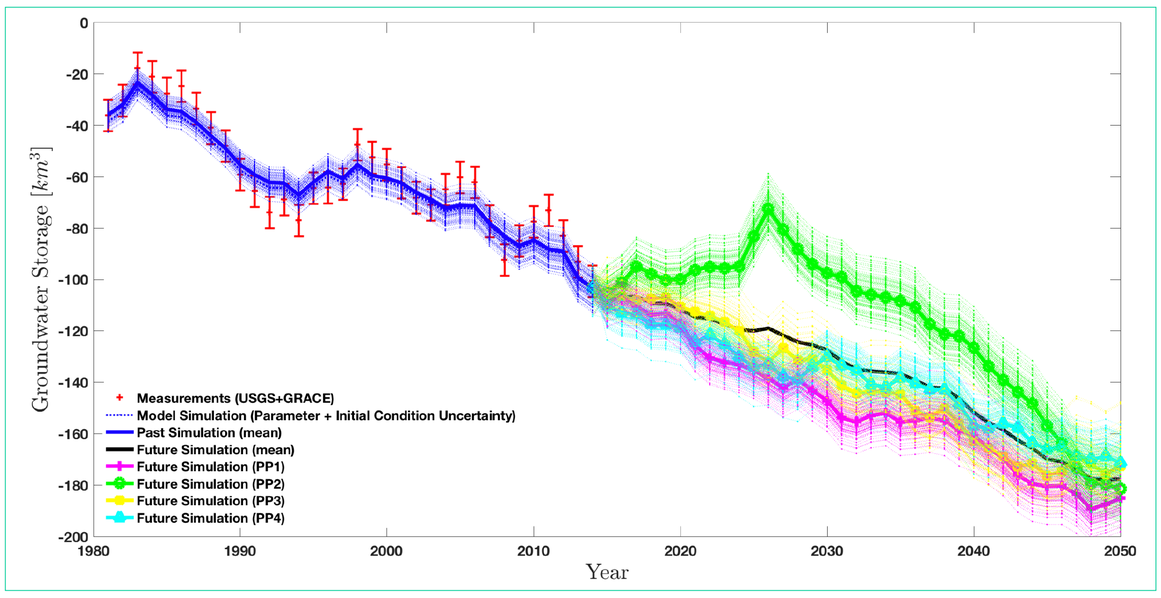

Fig.7 (Bottom) We then run the model with different management strategies. For this, we run the model with 20% changes of in each demand/supply variable, to examine sensitivity of groundwater storage to each variable. Model results show that increases in surface water supply and agriculture efficiency have a stronger potential to stabilize groundwater storage compared to urban water use efficiency and increased supply from recycle and reuse.

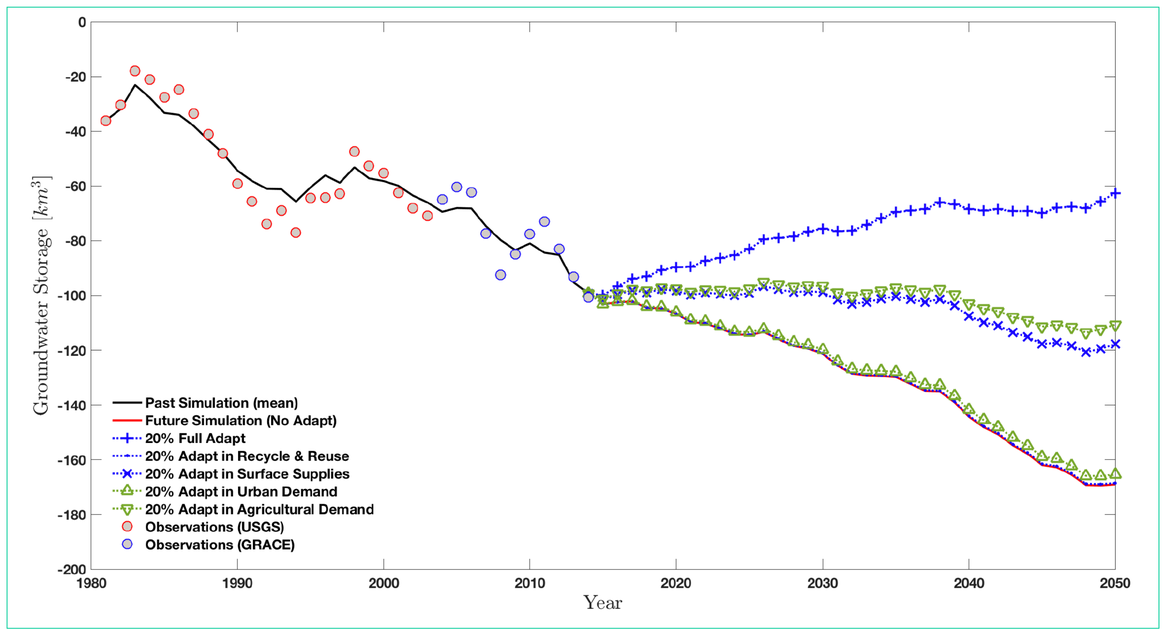

Main Conclusion: It is clear that a comprehensive approach looking at both supply and demand side management strategies may be necessary to sustain groundwater levels in the future.

Presenter: Elias C. Massoud
elias.massoud@jpl.nasa.gov

Poster No. EA 11

National Aeronautics and Space Administration
Jet Propulsion Laboratory
California Institute of Technology
Pasadena, California
www.nasa.gov

National Aeronautics and Space Administration

Optimal Inverse Estimation of Ecosystem Parameters from Observations of Carbon and Energy Fluxes

Debsunder Dutta (329G), Christian Frankenberg (329G) and David Schimel (329G)

1. Introduction

1. Canopy structural and leaf photosynthesis parameters such as leaf area index (LAI), maximum carboxylation capacity (V_{cmax}), and slope of the Ball-Berry stomatal conductance model (BB_{slope}) are crucial for modeling the canopy radiative transfer and plant physiological processes.

2. These key ecosystem parameters have seasonal variability, are difficult to measure in-situ, and represent large sources of uncertainty for predictions of carbon and water fluxes in ecosystem models.

3. Our hypothesis is that the inversion of detailed vertically resolved canopy model such as Soil Canopy Observation Photochemistry and Energy fluxes (SCOPE) with multiple canopy layers is able to retrieve the ecosystem parameters accurately using observations of carbon and energy fluxes

2. Objectives

1. Development of a conceptual Bayesian non-linear inversion framework using SCOPE for estimation of ecosystem parameters using eddy covariance flux observations.

2. Demonstrating the retrieval and posterior error reduction of key ecosystem parameters using observations of carbon and water fluxes across different ecosystems.

3. Moving Window Inversion Framework using SCOPE

SCOPE is an integrated 1-D vertical radiative transfer and energy balance model. SCOPE utilizes the spectrally resolved visible to thermal (0.4 to 50 μm) infrared irradiation at the canopy top to derive the fluxes of water, energy, carbon dioxide and vertical profiles of temperature as a function of canopy structure and weather variables.

Linearization of forward model (SCOPE) is given as follows (X represents the state vector):

$$F(X;p) = F(X;p)_{X=X_l} + \left.\frac{\delta F}{\delta X}\right|_{X=X_l} (X - X_l)$$

In our case the cost-function is not perfectly quadratic, moreover the Jacobians are not constant making the problem non-linear and thus requires the stepwise Levenberg-Marquardt method for solution.

$$X_{i+1} = X_i + [(1+\gamma)S_a^{-1} + K_i^T S_\epsilon^{-1} K_i]^{-1}\{K_i^T S_\epsilon^{-1}[Y - F(X_i)] - S_a^{-1}[X_i - X_a]\}$$

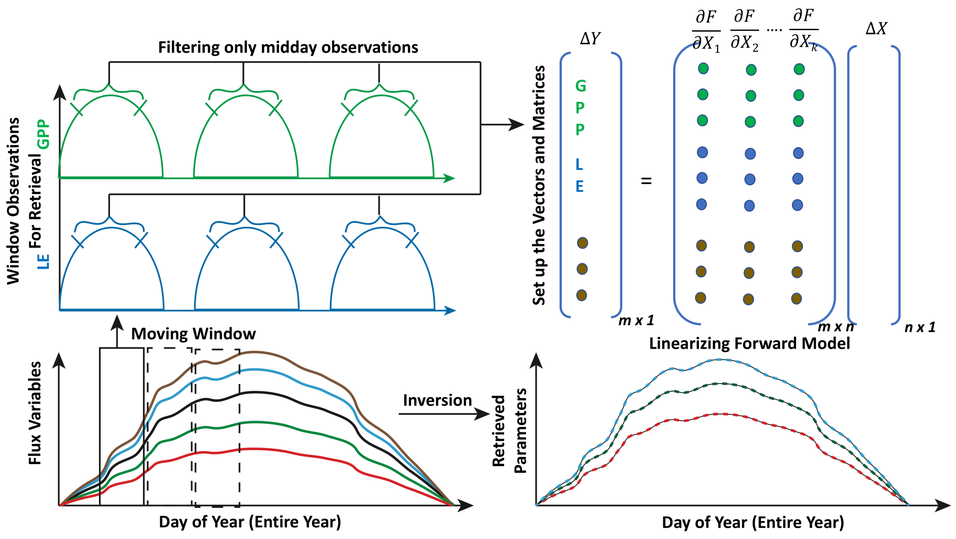

Fig.1 Illustration of moving window inversion retrieval setup. The bottom left part illustrates the ecosystem time series flux variables used for driving the SCOPE model. A n-day time window is selected for each retrieval in the yearly growing season and a time filter is implemented for concatenating the measurement vector in the retrieval windows. The top right shows the vector and matrix setup in the inversion framework. The bottom right shows the retrieved model parameters implementing the moving window approach.

1. The inversion is implemented in plain vanilla form current window to the next, with the estimated state vector (X) of the previous window as the first guess (but not prior) for the current window.
2. A convergence criteria is implemented based on the ratio of true error to the expected error for each iteration step.
3. A purely diagonal prior error covariance matrix with zero off-diagonal elements are used for the retrievals.
4. The posterior error covariance matrix may contain off-diagonal elements indicating if the retrieved parameters are truly independent.

5. Results – Parameter Estimations

The Bayesian optimal inversion framework is applied to different ecosystems consisting of both C_3 and C_4 photosynthetic pathways:

1. Results for Nebraska Mead-1 Site with C_4 corn crops

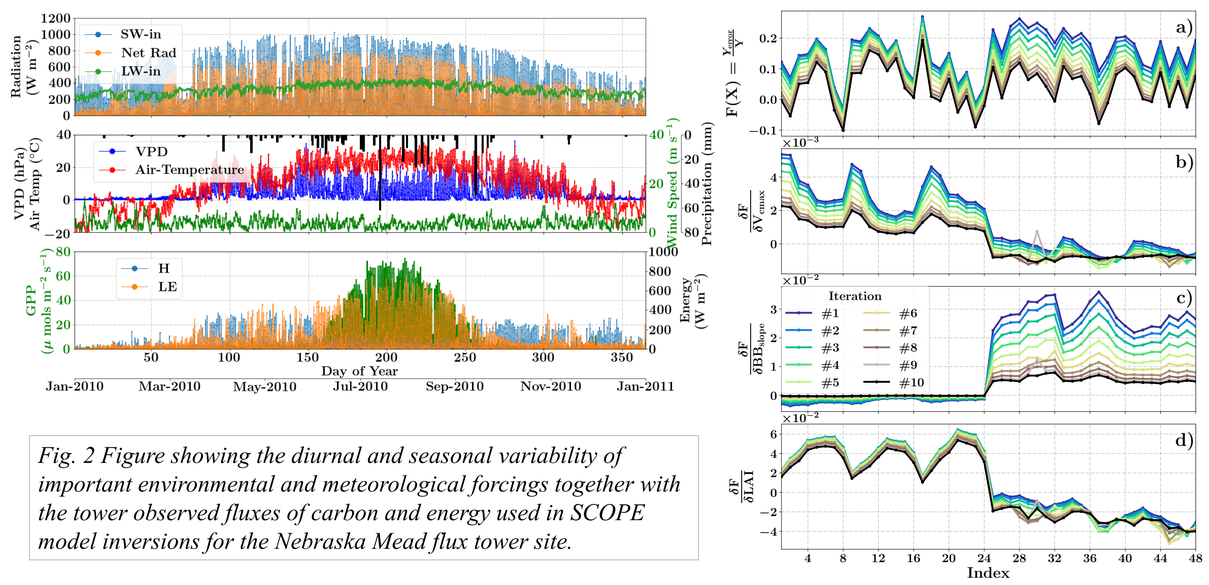

Fig. 2 Figure showing the diurnal and seasonal variability of important environmental and meteorological forcings together with the tower observed fluxes of carbon and energy used in SCOPE model inversions for the Nebraska Mead flux tower site.

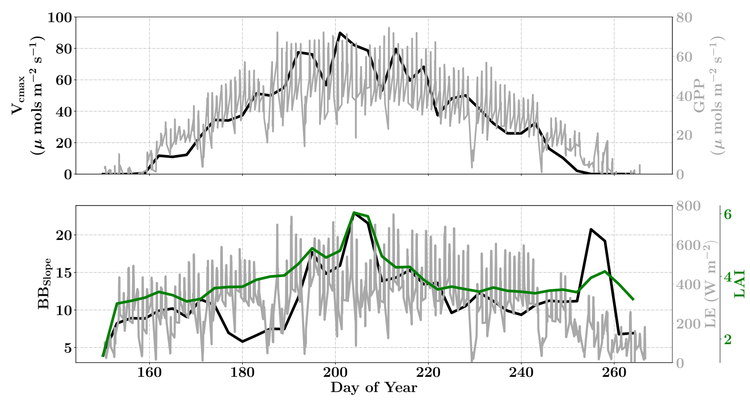

Fig. 4 Figure showing the seasonal variability in retrieved parameter values of V_{cmax}, BB_{slope} and LAI for the Nebraska Mead-1 site using a 3-day moving window inversion approach for the year 2010. The actual points in the time series (grey lines) of the GPP and LE fluxes used as the target observations (Y) for the moving window inversion approach are shown in the background.

Fig. 3 Figure showing the evolution of the Jacobian Matrix for one retrieval window (DOY 213-216) for the Nebraska Mead-1 site in 2010. The normalized mismatch Y_{error} between the observation and modeled vector (observed minus modeled) for the 3-day window composed of GPP (indices 1-24) and LE (indices 25-48) time series concatenated together for each retrieval iteration is shown in panel (a). The normalized gradients of the forward model (SCOPE) with respect to the variables in the state vector after each update step of the LM algorithm are shown in the panels (b), (c) and (d) respectively. The gradient decreases with each iteration and the observations of GPP are weighed more for V_{cmax}, Observations of LE more for BB_{slope} and both for the LAI retrievals.

2. Results for Missouri Ozark Site with C_3 deciduous vegetation

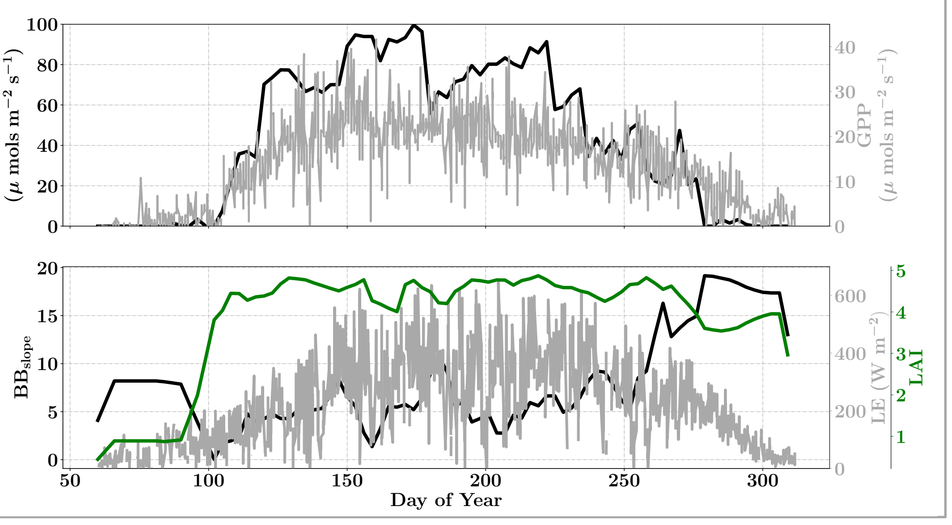

Fig. 5 Figure showing the seasonal variability in retrieved parameter values of V_{cmax}, BB_{slope} and LAI for the Missouri Ozark site using a 3-day moving window inversion approach for the year 2010.

5. Conclusions

1. Bayesian moving window inversion approach successfully retrieves key ecosystem parameters by constraining the SCOPE modeled carbon and water fluxes using eddy-covariance flux observations.
2. Our model inversion results well captures the seasonal variability in the parameters in alignment with evidence from measurements .
3. The developed framework is flexible to incorporate other (and any number of) constraining measurements such as sun induced fluorescence, visible to shortwave reflectance, etc for estimating a range of physiological parameters such as chlorophyll content, entropies and activation energies of photosynthetic temperature dependence parameters.

National Aeronautics and Space Administration

Jet Propulsion Laboratory
California Institute of Technology
Pasadena, California

www.nasa.gov

Poster No. EA-13

National Aeronautics and Space Administration

Lidar detection of tropical forest degradation through simulations of selective logging disturbance

Victoria Meyer (329G)
Sassan Saatchi (329G), António Ferraz (329G), Marcos Longo (329G), Michael Keller (329G)

Introduction

Developing countries are required to report their carbon emissions to benefit from UN-REDD* programs. They need tools to accurately evaluate the state of their forests. Forest degradation is a disturbance due to anthropogenic changes and is considered a major source of carbon emissions. Unlike deforestation, forest degradation is difficult to detect, especially selective logging. The **detectability** and thus the **impact of logging** are therefore poorly understood.

Here, we simulate various intensities of selective logging based on a small footprint Lidar point cloud in a 50ha area in Barro Colorado Island, Panama. The goal is to determine if logging can be detected using a single dataset, without information on pre- and post-logging activities.

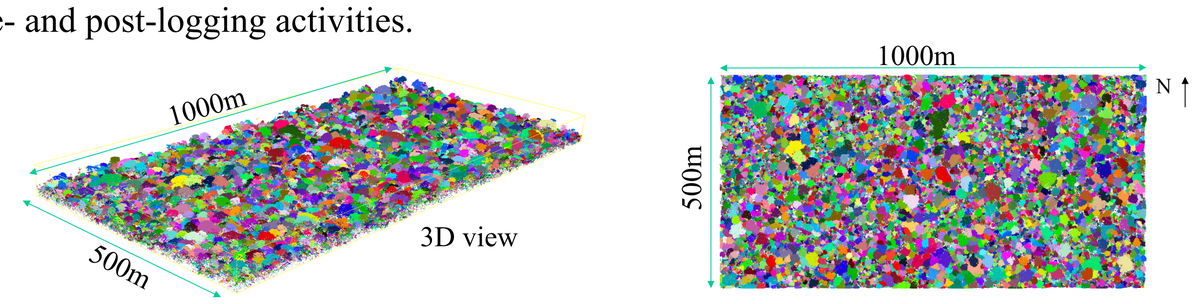

Individual Tree Crown (ITC) detection in a 50ha plot, based on Ferraz et al., 2016. All points belonging to the same tree are assigned the same color for visualization purposes. Point density: 10pts/m^2

Degradation Simulation

Logging simulation parameters are based on a published study reporting on roads, loading decks ,skid trails and gap damage from a selectively logged forest in Brazil (Feldpausch et al., 2005). The whole process is automated.

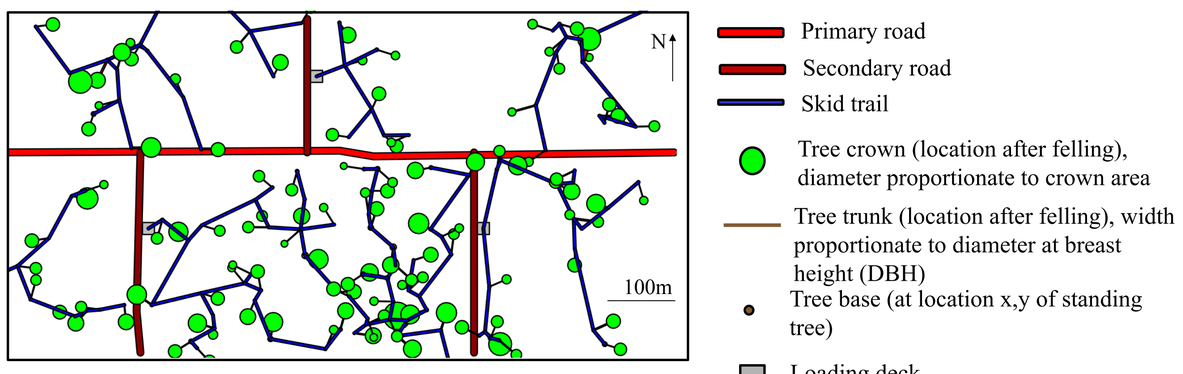

50ha plot as seen from above, with 2.2 logged trees/ha

Road width: 8m, avoiding trees>40m
Deck size: 340m^2
Deck density: 0.06/ha
Skid trail width: 4m, (max H=20m), optimized paths connecting trees, leading to decks.

Logged trees: 2.2 tree/ha (chosen randomly), DBH>60cm (or H>30m), gap damage around the crown and along the fallen trunk
Felling direction: random
Terrain: Flat: topography not taken into account.

The location of the trees to be harvested and the direction of their felling are random, allowing for multiple simulations (n=100) for robust results.

Validation of method

The simulation results were tested against the results reported in the reference study (Feldpausch et al., 2005), for the same logging intensity (2.2 trees/ha).

	Lidar_simulation	Reference	Validation
Roads			
N trees/ha	14.8	5	Higher road density
mean DBH ± sd	23.5 ± 21.8	-	
Decks			
N trees/ha	0.9	1	✓
mean DBH ± sd	28.7 ± 38.9	-	
Skid Trails			
N trees/ha	10.32	12	✓
mean DBH ± sd	15± 12.1	14 - 18	✓
Felling (collateral damage)			
N trees/ha	13.82	13-25	✓
mean DBH ± sd	14.9 ± 13.4	18 - 19	✓

The simulation gives similar results in terms of number of trees removed (roads, decks, skid rows) and crushed (felling), and their diameter range. This validation was necessary to proceed and test other logging intensities scenarios.

Results

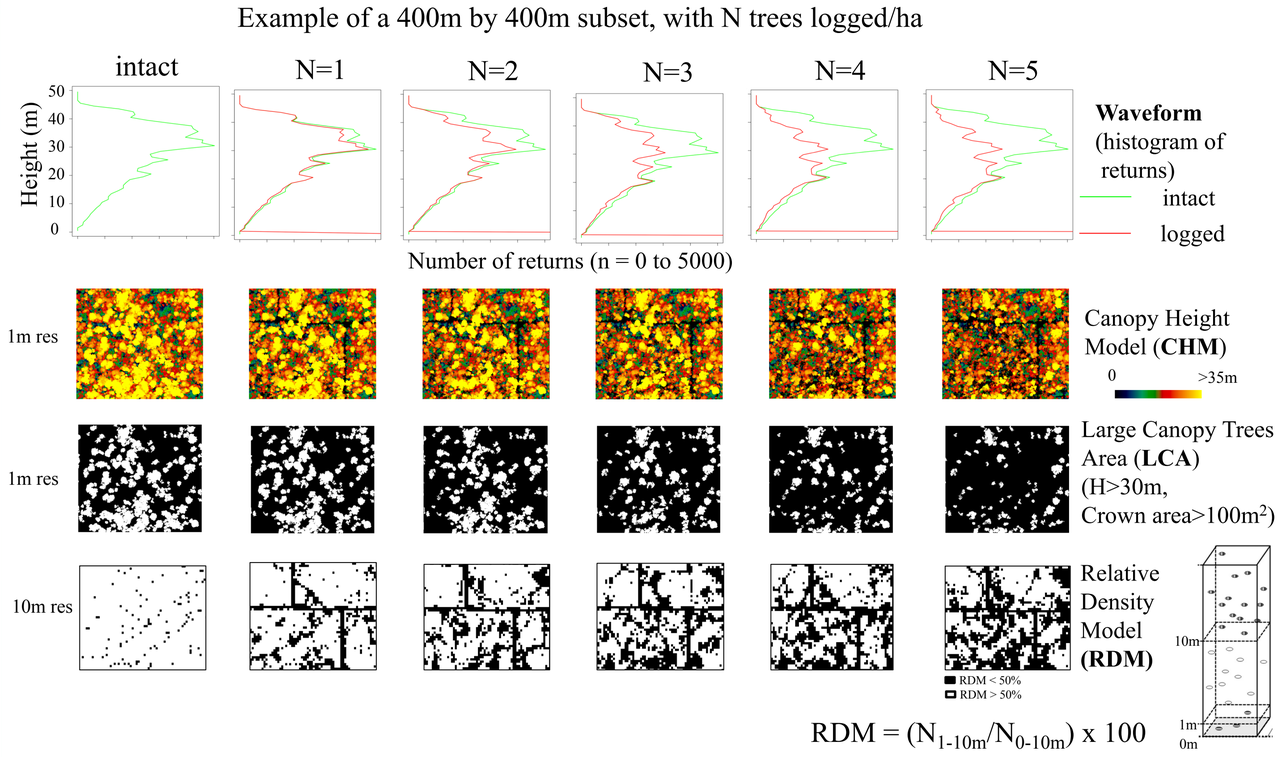

Logging mainly impacted the higher part of the waveforms (>25m). This might be exaggerated by the fact that there are less Lidar returns in the lower part of the vertical structure of the forest. Skid trails are only detected using RDM and don't affect the canopy.

Allometric equation from Meyer et al., 2018

Impact of logging on biomass estimation and forest structure based on 50 plots of 1ha. Results for logged scenarios were obtained by repeating the simulation 100 times. MCH: Mean top Canopy Height.

Biomass loss based on MCH is not significant until more than 2 trees/ha are logged. This suggests that low intensity logging activities don't have a significant impact on biomass loss. RDM change becomes significant at 1 logged tree/ha.

Conclusion

Our approach is able to simulate forest degradation with similar results reported in the literature based on field data.
Although low intensity logging is detectable with RDM, it has a non-significant impact on biomass loss, provided that the logging intensity is below 2 trees/ha.
Biomass loss from more intensive logging activities can be detected if the mean and standard deviation of the forest structure (MCH, LCA, RDM) are known.

Future work and other applications

Forest regrowth will be added to the simulation, allowing for detection of degradation through time.
This new methodology can be modified and applied to any kind of disturbance, including natural (blow out, drought) and anthropogenic (fires, deforestation) disturbances, providing a powerful tool to understand and predict the impact of such events.

National Aeronautics and Space Administration
Jet Propulsion Laboratory
California Institute of Technology
Pasadena, California

*United Nations Collaborative Programme on Reducing Emissions from Deforestation and Forest Degradation in Developing Countries

www.nasa.gov

Poster No. EA-14

National Aeronautics and Space Administration

Dust sources in North Africa and Middle East determined from MISR satellite observations

Author: Yan Yu (329J-Affiliate)
Olga V. Kalashnikova (329J), Michael J. Garay (329J), Huikyo Lee (398L)

Introduction

- North Africa and Middle East: global dust hotspots.
- Inconsistent dust source maps from current satellite-based dust source identification approaches due to their own limitations:
  - **Aerosol loading approach** dust source = high aerosol loadings, detected by e.g. satellite aerosol optical depth (AOD) – rely on retrieval assumptions, saturates at high AOD values.
  - **Dust tracking approach** tracks dust plumes based on Brightness Temperature difference detected by geostationary satellite instruments – miss-classification between desert surface, dust, and clouds.
- Substantial increase in AOD over the Middle East since the onset of the 21st century has been revealed from various observations, but remains unclear (1) if it is a long-term trend and (2) what is the source.

Objective

- Combine a novel plume-motion with the dust-loading approaches to identify dust sources in the North Africa and Middle East.
- Revisit the recent trends and interannual variability in dust activation and dust concentration in the North Africa and Middle East.

Method

- **Plume-motion**: dust plume height and motion in the cloud motion vector product (CMVP) provided by Multi-angle Imaging SpectroRadiometer (MISR) aboard the polar-orbing Terra satellite
  - Geometrically derived, no saturation problem.
  - A "dust activation event" is identified when the dust plume moves faster than 10 m s-1 and the plume top height is within 2 km of the ground.
- **Dust-loading**: MISR nonspherical (dust) AOD (DAOD)
  - MISR detects particle shape classes.
  - Dust is the primary nonspherical aerosol particle especially over deserts.

Seasonality in dust activation and concentration is driven by wind speed and precipitation.

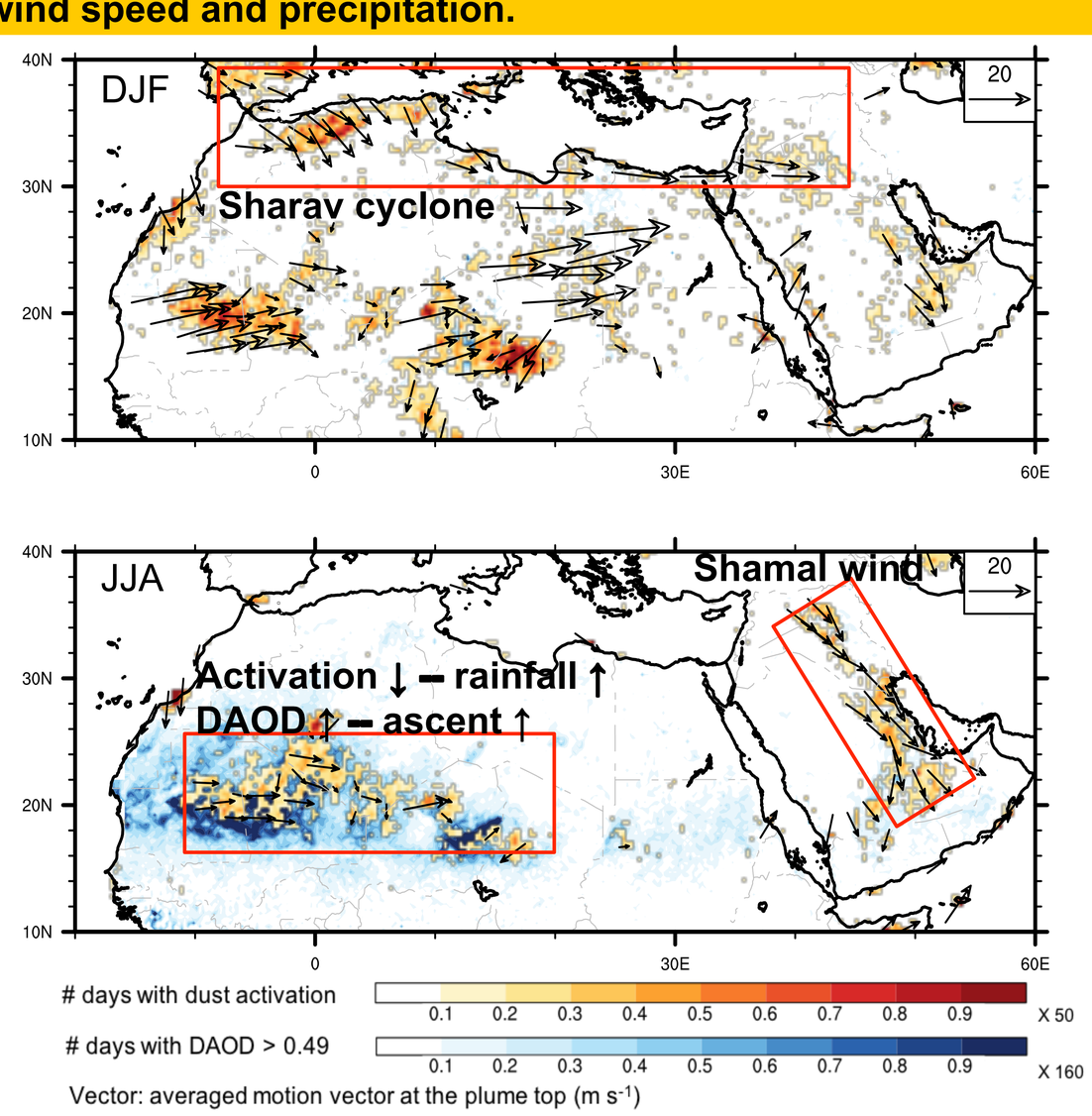

Maximum trend during 10-year sub-periods (2001-2010, 2002-2011, etc) confirms the substantial increase in Middle Eastern dust concentration, mainly due to local sources.

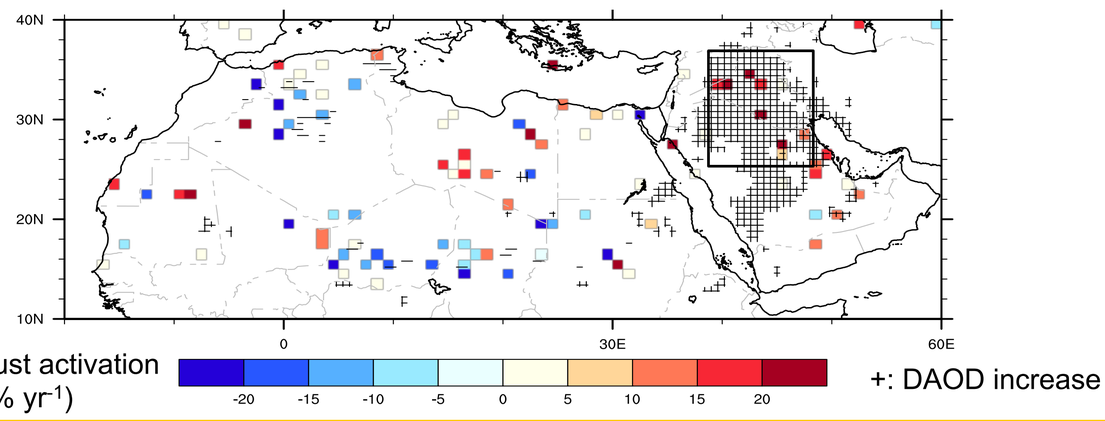

In response to precipitation and vegetation, dust activation and DAOD increased during 2001-2012 but recovered afterwards

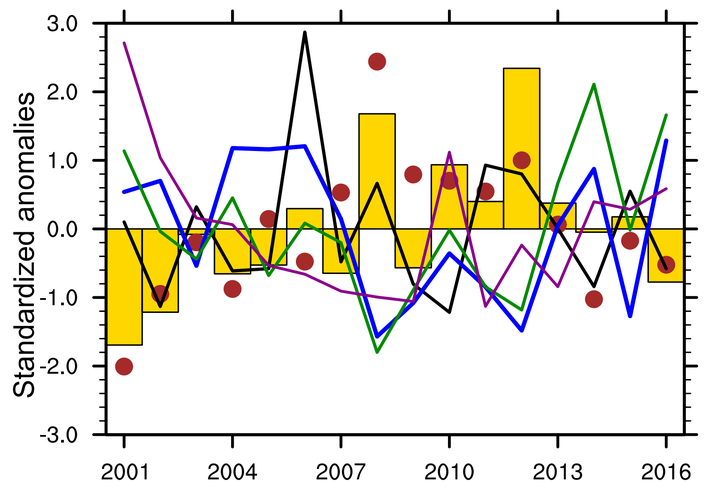

Rank corr (* significant)	Dust activation	DAOD
Frequency of High Wind Speed	0.45	0.26
15-month Precipitation	-0.60*	-0.71*
Amount of vegetation	-0.52*	-0.82*

MISR CMVP identifies dust sources at geographical depressions.

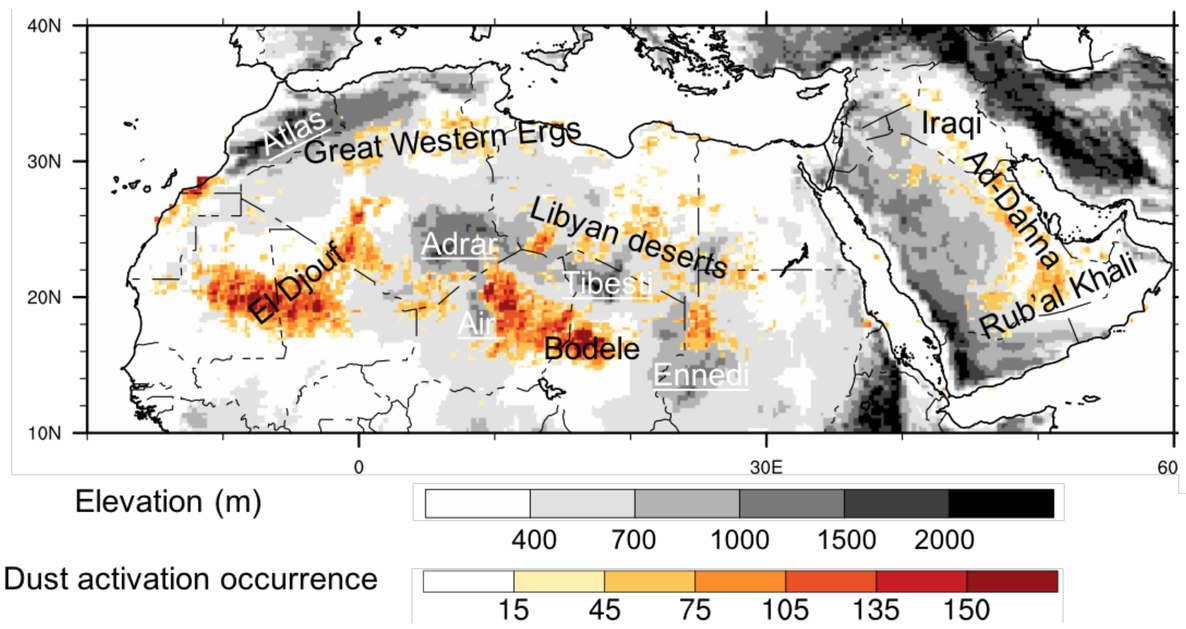

- The West African deserts are active dust sources according to MISR CMVP but not according to previous AOD-based approach.
- West African dust storms are often characterized by optically thick dust walls, which cannot be retrieved using aerosol-loading approaches.

- **In summary, the MISR CMVP approach provides an encouraging and independent complement for the aerosol loading-based or dust-tracking approaches to identify dust source regions.**
- **Future studies are encouraged that combine different dust source identification approaches to generate a more accurate dust source map, which will improve dust and climate modeling.**

National Aeronautics and Space Administration
Jet Propulsion Laboratory
California Institute of Technology
Pasadena, California

www.nasa.gov

Poster No. EA-15

National Aeronautics and Space Administration

Superpixel Change Detection for Synthetic Aperture Radar

Charlie Marshak (334F)
Marc Simard (334F)

Introduction

- The upcoming **NASA-ISRO SAR** (NISAR) mission will provide dense temporal sampling of high resolution L-, S-band SAR imagery.
- Data will improve estimates of above ground biomass and global carbon stocks for carbon cycle models [1].
- Rapid sampling (12-day repeat pass) will allow for improved monitoring of above ground biomass, wetland inundation, and agricultural changes.
- L-band HV backscatter is useful for monitoring forest disturbances without atmospheric interference. The NISAR science requirement is to detect 80% of regions with at least 50% of forest loss [1].
- Dense temporal sampling permits differentiation between temporary seasonal changes and enduring forest disturbances.
- According to NISAR's Algorithmic Theoretical Basis Document (ATBD) [1], forest disturbance is measured using changes to average backscatter within square regions, though these square regions need not respect natural image boundaries.

Objective

- Introduce algorithm to process multiple spatial and temporal scales and identify enduring changes in L-band SAR imagery. Utilize powerful computer vision tool known as superpixels.
- Demonstrate methodology using *open source* python tools [2, 3].
- Compare new methodology to the existing change detection proposed in ATBD using ALOS-1 L-band images.

Superpixels

Superpixels are contiguous image segments; we use the method from [4]. We use superpixels to reduce *speckle noise* and *track regions* with similar HV backscatter.

Methodology

1. Select focal image to analyze within co-registered stack.
2. Select window of older and more recent states to compare to focal image.
3. Form difference stack using the images within the window.
4. Extract superpixels from the difference stack.
5. Aggregate backscatter within a superpixel using the mean or median and apply to each difference image in stack.
6. Threshold aggregated backscatter differences to identify change.
7. Create change map:
   - Including change that persisted in more recent states
   - Exclude any change that occurred in any previous state

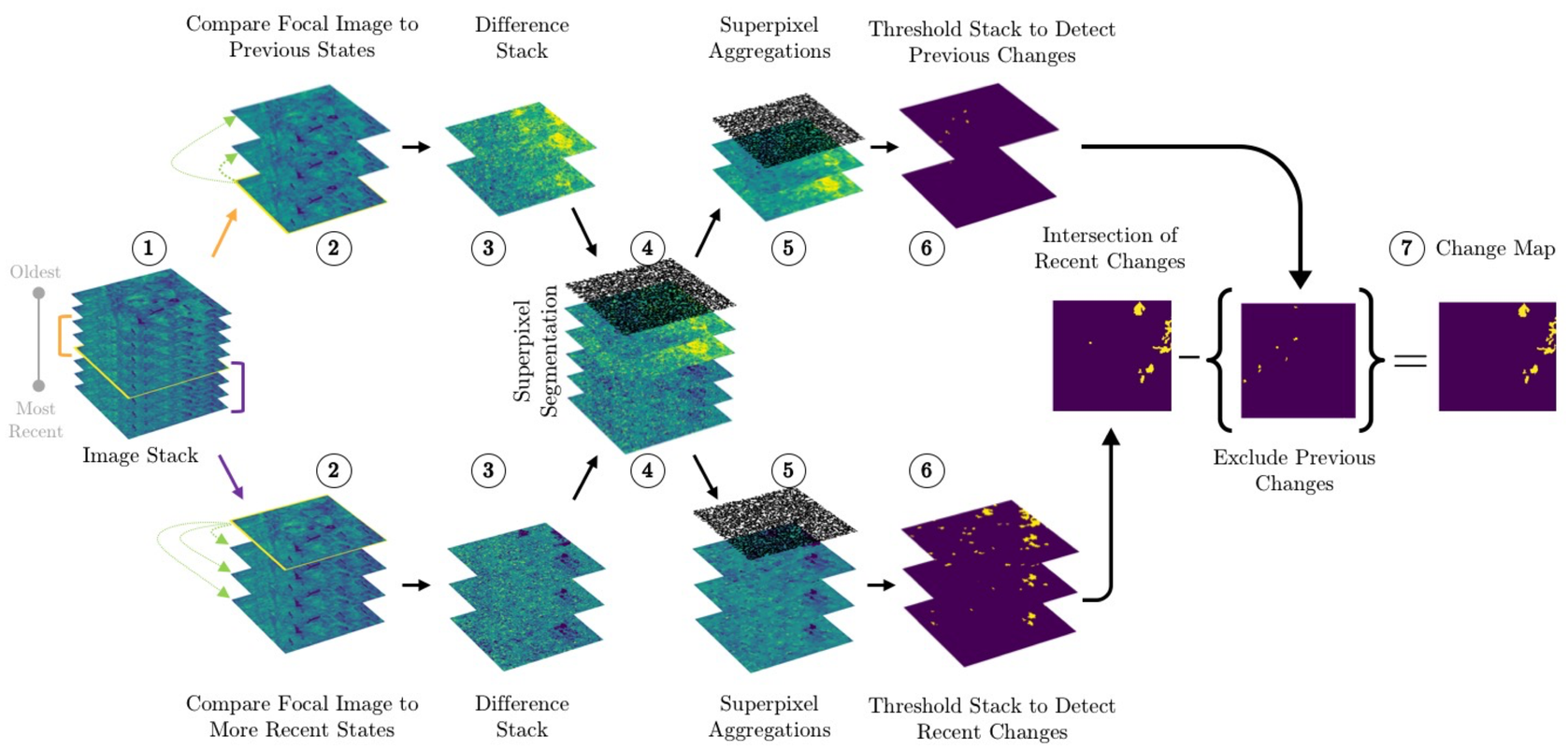

Results and Future Work

- Tested methodology on ALOS-1 L-band imagery over Laurentides Wildlife Reserve in Quebec, Canada (Left panel of Figure), which is a Cal/Val site [1].
  - Hand labeled data on image stack as proxy to true forest loss.
  - Our proposed method out performed pixelwise thresholding and averaging in square regions (see center panel of Figure).
  - We compared performance using the F_1 score (harmonic mean of producer and user accuracies).
- Created python package with numerous Jupyter notebooks to explain usage.
- Plan to implement product to quantify uncertainty and improve data validation.

Figure (Left) Study area in Laurentides Wildlife Reserve. (Center) F_1 scores for various thresholds and change detection methods. (Right) Confusion matrix of change map obtained from our methodology using threshold with highest F_1 Score.

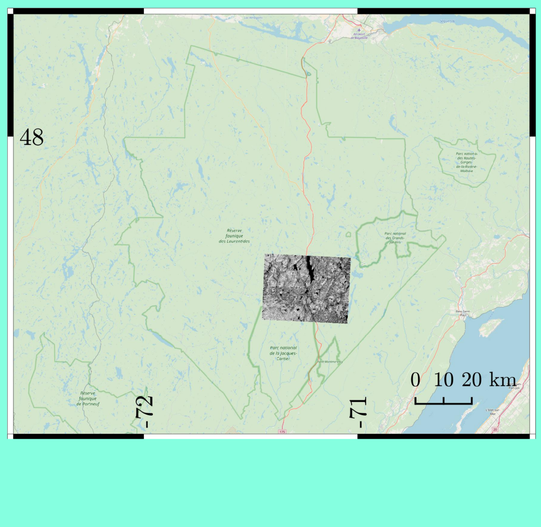

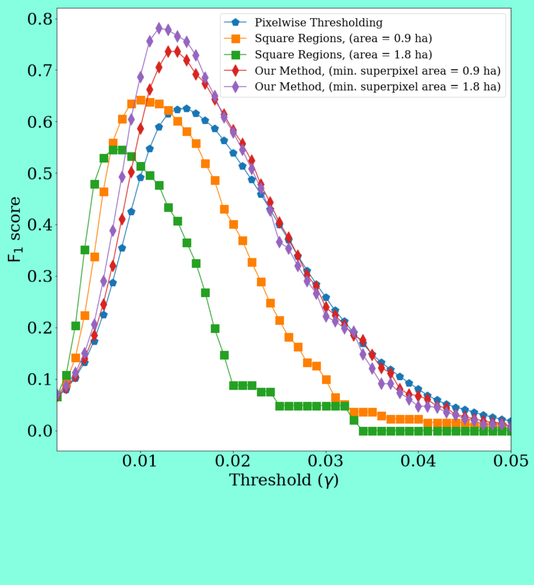

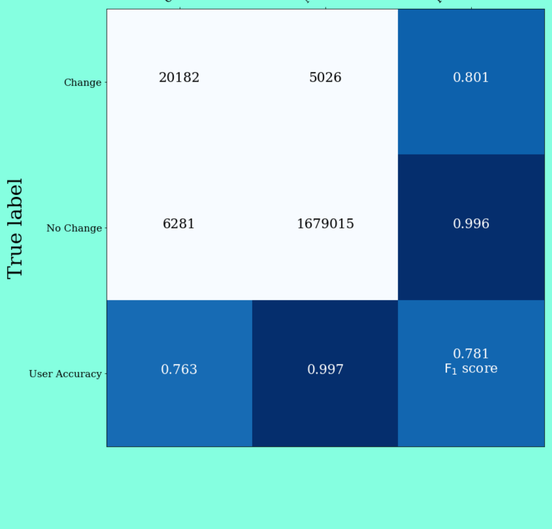

National Aeronautics and Space Administration

Jet Propulsion Laboratory
California Institute of Technology
Pasadena, California

www.nasa.gov

References

[1] Jet Propulsion Laboratory. NASA-ISRO SAR (NISAR) Mission Science Users' Handbook (2017).
[2] Sean Gilles and Rasterio contributors. *Rasterio* (2013). GitHub repository, https://github.com/mapbox/rasterio.
[3] Stéfan van der Walt, Johannes L. Schönberger, Juan Nunez-Iglesias, François Boulogne, Joshua D. Warner, Neil Yager, Emmanuelle Gouillart, Tony Yu and the Scikit-Image contributors. "Scikit-Image: Image Processing in Python." PeerJ 2:e453 (2014) http://dx.doi.org/10.7717/peerj.453
[4] Pedro F. Felzenszwalb and Daniel P. Huttenlocher. "Efficient graph-based image segmentation." *International Journal of Computer Vision* 59.2 (2004): 167-181.

Poster No. EA-16

National Aeronautics and Space Administration

The potential of Polarimetric Radio Occultations in the thermodynamic characterization of heavy precipitation

Ramon Padullés (334H)

F. J. Turk (334H), C. O. Ao (335G) and M. de la Torre-Juárez (3222)

Incomplete understanding of the **role of water vapor** driving **heavy precipitation** lead to **large disparities** in the representation of such events among different current climate models. In this context, the role of **observations** is to provide **simple and reliable relationships** between thermodynamic observable quantities to assess model's performance in representing such processes, reducing uncertainties, and to **better understand the thermodynamics** underlying heavy precipitation.

Polarimetric GNSS Radio Occultations (GNSS PRO)

Polarimetric GNSS RO will provide, **for the first time**, **joint** products of **vertical thermodynamic profiles** and **vertical precipitation information**.

Signals emitted by GNSS satellites are collected on a Low Earth Orbiter in occulting geometry. The signals, as they penetrate into the lower layers of the atmosphere, bent. The bending can be inferred from precise phase delay measurements, and associated to vertical gradients of the Earth's atmosphere refractivity. **Temperature, Pressure and Water Vapor** are finally obtained from the vertical refractivity profiles.

Falling heavy precipitation raindrops become asymmetric, inducing a differential phase delay between the linear orthogonal components of propagating electromagnetic waves. Precipitation information is obtained from the **along-ray integrated phase delay** between the Horizontal and Vertical components of the propagating electromagnetic GNSS signal.

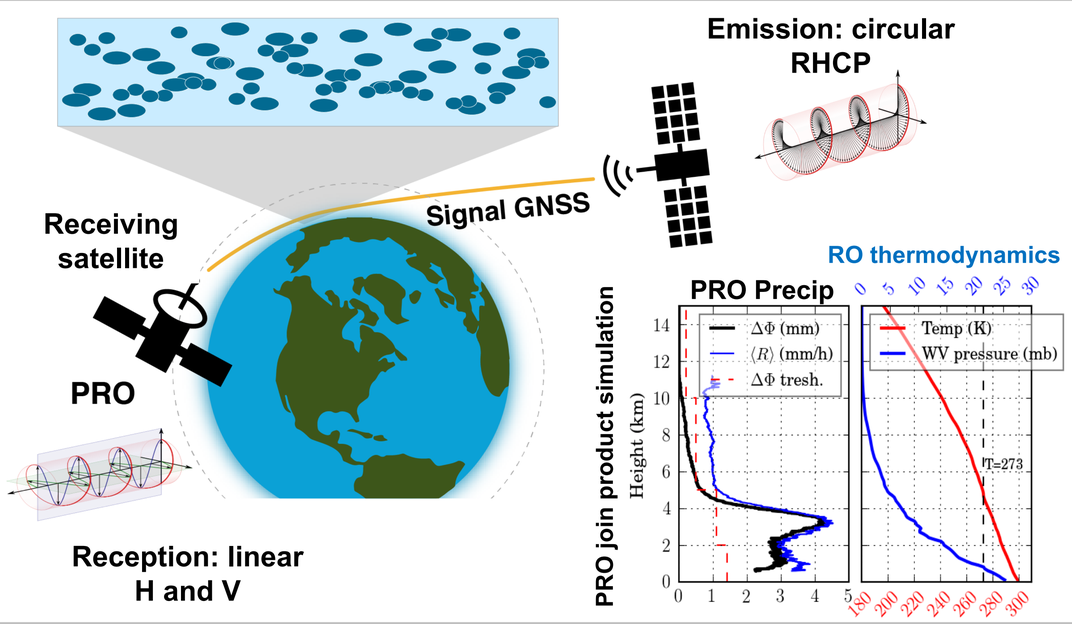

RO observations vs model (re) analyses

COSMIC standard RO observations **co-located** with analyses and re-analyses (ERA-Interim, ECMWF High Resolution and NCEP GFS) are used to assess the bias between RO **refractivity** and that of analyses, in the **free troposphere**, when heavy precipitation is present. Precip data from GPM IMERG products (0.1° x 0.1°; 30 min; 1D).

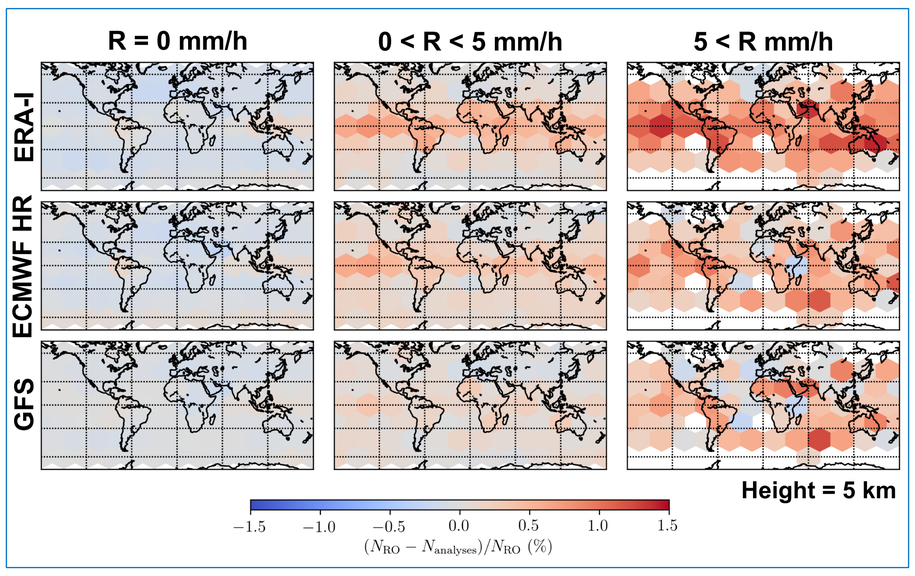

This difference is shown to be correlated with high specific humidity rather than with precipitation scattering, therefore indicating the **issues of models/analyses** treating free tropospheric humidity, specially within heavy precipitation.

Vertical precipitation characterization using existing standard RO observations

While PRO obs. are **not yet available**, we use **coincident** COSMIC / Metop A & B standard RO products with GPM IMERG precipitation data to build **precipitation transition statistics**. Moisture positioned above boundary layer (free troposphere, 850-200 mb) has been shown to play an important role in the **onset of heavy precipitation**, and **here it is confirmed for different regions using actual RO observations**. It is also shown how the **partial (free tropospheric) integrated column water vapor** critical value, at which precipitation exhibit a sharp pickup, depends on the temperature.

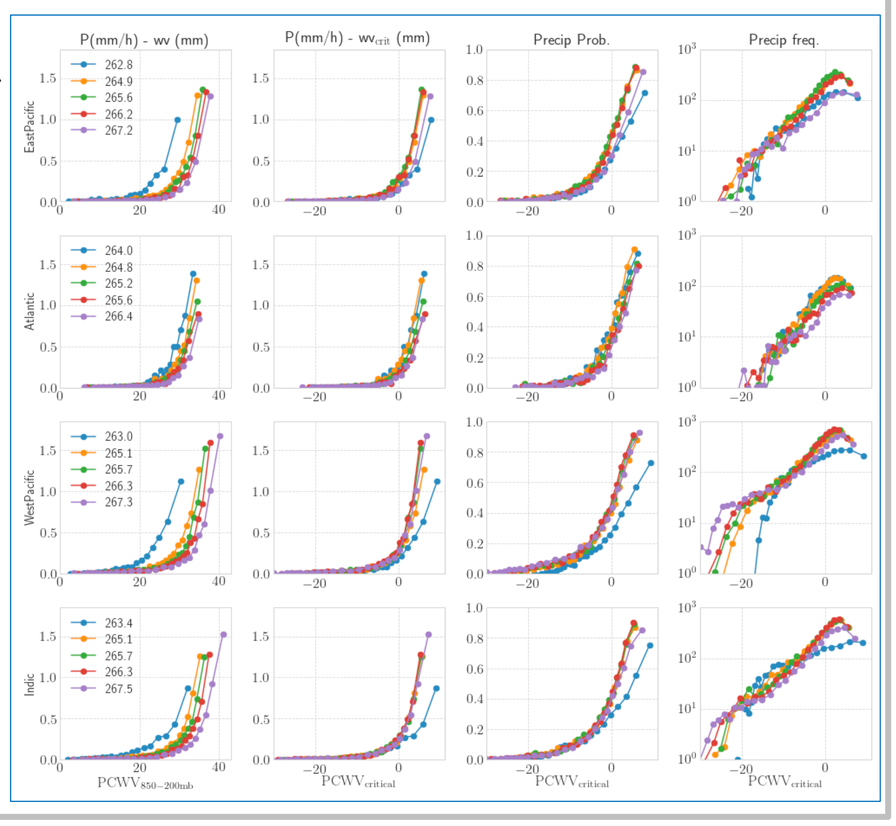

Conclusions and impact

- RO observations are shown to be a **powerful tool** in the study of the **vertical thermodynamic structure** of precipitation, providing precipitation transition statistics comparable to those already obtained with radiosondes, and being able to spatially expand these **observable relationships**.
- With **Polarimetric RO** we will be able to indicate the presence of precipitation, and to link the vertical thermodynamic profiles to the along ray (at each vertical level) precipitation contribution.
- Polarimetric RO are being collected **for the first time ever** on board the PAZ satellite, and the **data processing and analysis** has started successfully.

Initial Polarimetric Radio Occultation data assessment

The Radio Occultation and Heavy Precipitation onboard PAZ satellite experiment (ROHP-PAZ) is **collecting ROs at two polarizations (H, V) for the first time ever**. PAZ was launched on February 22, 2018, and the first PRO observations were received in May. An example of the SNR at two polarizations for one of the **first PRO observations ever** is shown below (left).

An important part of the cal/val phase of the experiment is to characterize the antenna pattern, modified from the original by a metallic structure included due to unexpected launcher changes. **Antenna pattern for H and V polarizations** are shown below (right). Only V-pol is enabled to sound the ionosphere (lower elevation). Zero azimuth corresponds to anti-velocity.

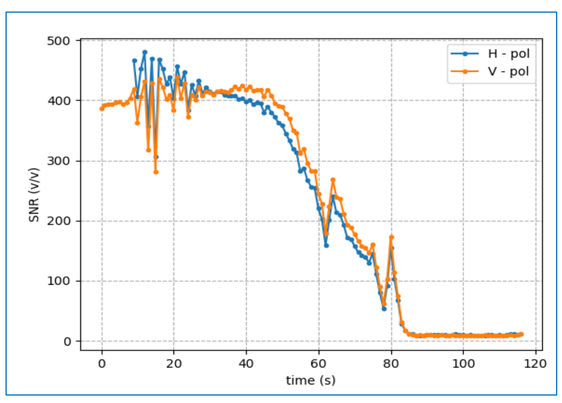

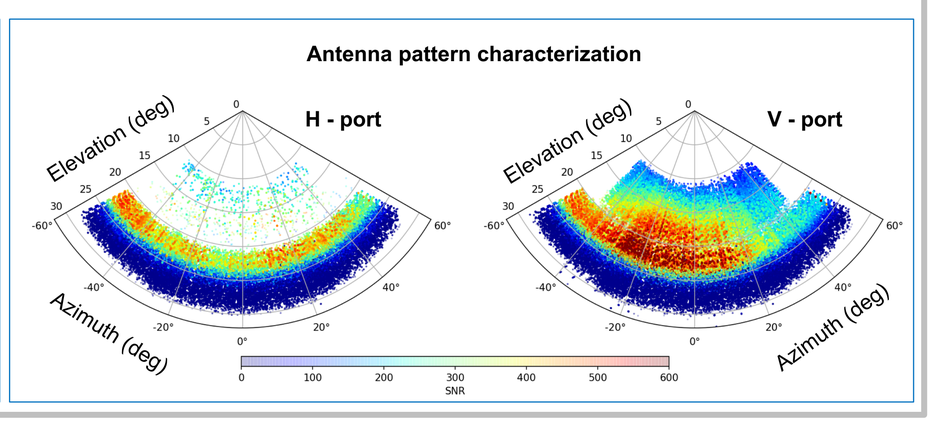

National Aeronautics and Space Administration

Jet Propulsion Laboratory
California Institute of Technology
Pasadena, California

www.nasa.gov

Padullés et al. 2018, *ACP Discussions*, 10.5194/acp-2018-66; **Cardellach et al**. 2017, *Quarterly Journal of the Royal Meteorological Society*, 10.1002/qj.3161; **Schiro et al. 2016**, *Journal of the Atmospheric Sciences, 10.1175/JAS-D-16-0119.1*; **Holloway & Neelin**, 2009, *Journal of the Atmospheric Sciences*, 10.1175/2008JAS2806.1; **Neelin et al**. 2009, *Journal of the Atmospheric Sciences,* 10.1175/2009JAS2962.1

Poster No. EA-17